Thermodynamic Modeling of Phase Behavior in Shale Media

Zhehui Jin, RERI, and **Abbas Firoozabadi,** RERI and Yale University

Summary

In conventional permeable media, once pore volume (PV) is known, the amount of fluid-in-place can be estimated. This is because the fluid is locally homogeneous, pores are generally larger than 100 nm, and surface adsorption is negligible. In shale media, in addition to PV, knowledge of pore-size distribution, total organic content, and chemistry of the rock is required. Fluid molecules in shale media can be found in three different states: (1) free molecules in the pores, (2) adsorbed molecules on the pore surface, and (3) dissolved molecules in the organic matter. Of the three, the first two mechanisms are discussed in the literature. In this work, we compute for the first time the amount of dissolved molecules.

To compute the fluids in shale media, we divide the pores into sizes greater than 10 nm and sizes less than 10 nm. In pores greater than 10 nm, the interface curvature affects phase behavior, and fluid phases are homogeneous. Therefore, they can be described by conventional equations of state. Our calculations show that retrograde condensation increases in nanopores; the upper dewpoint increases, and the lower dewpoint decreases. These calculations are supported by experimental measurements. Gas solubility in water and liquid normal decane shows a modest increase with curvature.

In pores less than 10 nm, the fluids become inhomogeneous, and the direct use of conventional equations of state cannot be applied even with adjusted critical pressure and temperature. We suggest the use of molecular modeling. A model such as the Langmuir adsorption isotherm is merely a curve fitting of the data.

We use available data in shale media, which are mainly limited to excess sorption of methane and carbon dioxide, to compare to our thermodynamic model computations. This is the first attempt to compare measured data in shale and predictions that are based on the integration of molecular modeling and classical thermodynamic modeling.

Introduction

Production from shale gas and shale light-oil reservoirs has dramatically increased during the past few years and has stimulated profound interest in exploration and production activities (Gasparik et al. 2012). Recovery and production from shale reservoirs depend on fluid-in-place and transport in shale media (Gasparik et al. 2013). The issues of the fluid-in-place and transport have been a mystery. The common belief is that the fluid stored in shale is mainly composed of free fluid molecules in pores and fractures and adsorbed fluid molecules associated with organic and mineral constituents of the rock (Gasparik et al. 2012). The amount of free molecules is mainly determined by porosity; adsorbed molecules are related to surface area in shale rocks. The organic matter provides porosity; it also has micropore structure that facilitates adsorption (Zhang et al. 2012). There is a strong correlation between the organic matter of the shale, often expressed as the total organic carbon, and fluid contents (Manger et al. 1991; Lu et al. 1995; Ross and Bustin 2007; Strapoc et al. 2010; Weniger et al. 2010). The inorganic part of shale such as clay minerals has micropore-to-mesopore structures that provide additional surface area for sorption. The adsorption depends on the pore structure and rock chemical composition (Ross and Bustin 2009; Jin and Firoozabadi 2013). Clay minerals are hydrophilic. As a result, water can readily occupy the adsorption sites and may greatly reduce adsorption of other species (Ji et al. 2012; Jin and Firoozabadi 2014).

In addition to free molecules and adsorbed species, there have been reports indicating that fluid dissolution in kerogen may also contribute to fluid content in shale permeable media (Ross and Bustin 2009). Kerogen is the organic constituent of shale. The chemical composition of kerogen is similar to that of bitumen, which is semisolid with very high viscosity. Gases and liquids dissolve in bitumen, and the amount of dissolution increases as temperature decreases and pressure increases (Svrcek and Mehrotra 1982; Mehrotra and Svrcek 1988; Varet et al. 2013). Because of similarity of chemical composition of bitumen and kerogen, we suggest that light hydrocarbons and CO_2 may dissolve in kerogen. The dissolution in kerogen may provide an additional fluid-in-place mechanism. Bulk phase-equilibrium calculations were used to describe gas dissolution in bitumen (Mehrotra and Svrcek 1982; Mehrotra et al. 1985; Mehrotra et al. 1989; Jamaluddin et al. 1991). The dissolution in kerogen was briefly suggested by some authors. Kerogen is believed to consist of a crosslinked network of organic matter analogous to complex organic polymers and (Ertas et al. 2006; Kelemen et al. 2006) similar to coal. Crosslinked polymer networks can absorb significant amounts of gas and liquid solvents to swell (Larsen and Li 1994; Larsen and Li 1997a, b; Larsen 2004; Ottiger et al. 2008). Swelling behavior of coal is attributed to pure physical surface-adsorption process and absorption (dissolution) into coal matrix (Ottiger et al. 2008). However, characterization of the exact contribution from adsorption and dissolution in coal is challenging, because gas uptake would change pore and matrix structures. Regular solution theory and the Flory-Rehner model (Flory and Rehner 1943) were used to study swelling behavior of kerogen (Larsen and Li 1994; Larsen and Li 1997a, b; Ertas et al. 2006; Kelemen et al. 2006). In this empirical approach, the nature of adsorption, dissolution, and specific interactions between the solvent and matrix are not modeled. The solubility parameter, crosslink density, and native swelling fraction are used to match the experimental data. When solubility parameters of solvents and kerogen are close, swelling is maximum (Ertas et al. 2006; Kelemen et al. 2006). More thermally matured kerogen swells less (Kelemen et al. 2006). Recently, Etminan et al. (2014) measured methane dissolution in a shale sample with the batch-pressure-decay method and report as much as 20% of total fluid content to be from dissolution. The measured data have not been modeled yet.

There are two main approaches in phase-behavior modeling in shale media: Langmuir adsorption isotherm and cubic equations of state (EOS). Before proceeding to our modeling of phase behavior in shale nanopores, we discuss these two approaches.

Langmuir Adsorption Isotherm. This isotherm has been suggested to describe adsorption in shale media (Ambrose et al. 2010; Weniger et al. 2010; Vermylen 2011). The Langmuir adsorption model is based on the assumption that an ideal gas is in equilibrium with adsorbed species onto an idealized flat surface. Species are presumed to bind to distinct but equivalent sites

Original SPE manuscript received for review 4 March 2014. Revised manuscript received for review 19 March 2015. Paper (SPE 176015) peer approved 17 April 2015.

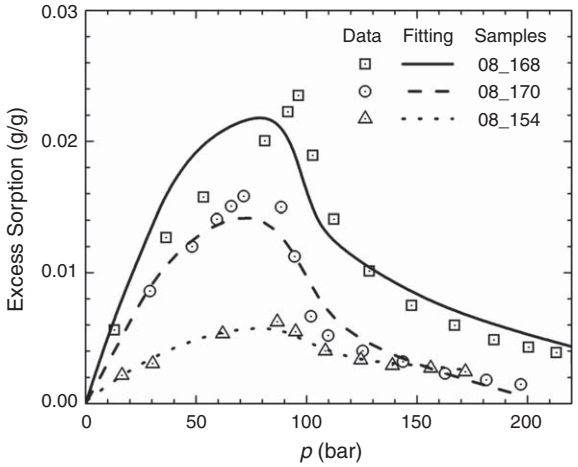

Fig. 1—Excess sorption of CO_2 in three different Irati shale samples at 318.15 K shows a nonmonotonic behavior that cannot be fitted with conventional Langmuir adsorption isotherms. Lines are from the modified Langmuir adsorption in Eq. 2 with an additional adjustable parameter. The data and fitting are adopted from Weniger et al. (2010).

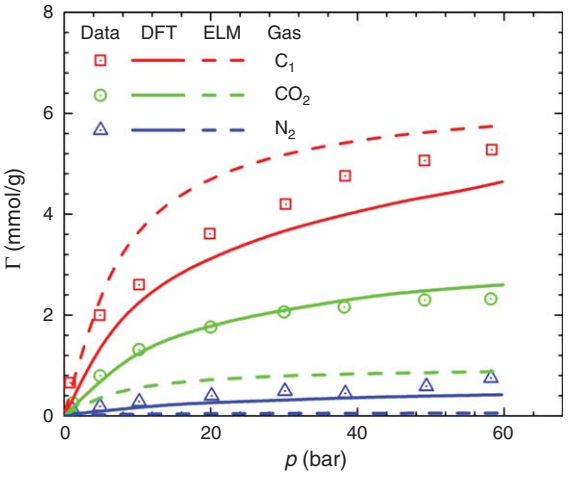

Fig. 2—Fluid content of ternary mixtures of C_1, CO_2, and N_2 (0.72/0.12/0.16, mole) in activated carbon at 298.15 K. Symbols are fluid content in activated carbon from experimental data (Dreisbach et al. 1999); solid lines are DFT predictions and dashed lines are the ELM.

on the surface. The Langmuir adsorption model is based on the assumption of a single adsorbed layer with no interaction among adsorbed species. The Langmuir isotherm for a single component is described by Das and Jonk (2012) as

$$V_a = \frac{V_L p}{p_L + p}, \quad \ldots\ldots\ldots\ldots\ldots\ldots\ldots\ldots\ldots\ldots\ldots\ldots\ldots\ldots (1)$$

where V_a is the adsorbed gas volume of bulk at pressure p, V_L is the maximum adsorption volume of bulk, and p_L represents the Langmuir pressure at which the amount of adsorbed gas content is $V_L/2$. The Langmuir adsorption expression may be used to describe sorption data of methane and carbon dioxide in porous media such as activated carbons (Dreisbach et al. 1999) and in some shale permeable media (Weniger et al. 2010). The expression does not relate to pore-size distribution (PSD). Langmuir adsorption is a limiting model for low pressure, and its application to the high-pressure adsorption isotherms cannot be justified (Weniger et al. 2010). Eq. 1 implies that adsorption monotonically increases with pressure and then reaches a plateau. However, data of Weniger et al. (2010) reveal that excess sorption of CO_2 in shale is nonmonotonic, as shown in **Fig. 1.** Excess sorption is defined as total fluids in the rock minus the amount of fluid that can fill the void volume on the basis of a homogeneous-fluid model. Note that all measurements are based on total fluid storage. The pore volume is measured with helium assuming no adsorption by pore filling (Weniger et al. 2010). We use the words "excess sorption" to include the effect from surface adsorption and dissolution in kerogen. Dissolution and absorption in the kerogen imply the same meaning, and the word "sorption" can refer to both adsorption onto the surface and absorption in kerogen. Most authors measure total fluid content, but they report excess sorption. The Langmuir adsorption isotherm is often used to describe excess sorption. There is no simple way to measure adsorbed molecules on the rock surface. An additional adjustable parameter, the density of adsorbed phase ρ_{adsorbed}, is introduced in the Langmuir adsorption isotherm to describe CO_2 excess sorption

$$V_a = \frac{V_L p}{p_L + p}\left(1 - \frac{\rho_{\text{bulk}}}{\rho_{\text{adsorbed}}}\right), \quad \ldots\ldots\ldots\ldots\ldots\ldots\ldots\ldots (2)$$

in which ρ_{bulk} is the density of bulk fluid phase. Three parameters V_L, p_L and ρ_{adsorbed} are obtained by fitting Eq. 2 to measured data. Weigner et al. (2010) argue correctly that the Langmuir adsorption isotherm is simply a curve fitting of experimental excess sorption data. In shale media, adsorption can be multilayer for small nanopores in kerogen source rocks and clay minerals. In addition, because of confinement, there may be capillary condensation and hysteresis. Langmuir isotherms cannot describe hysteresis, which is the difference between adsorption and desorption isotherms. Desorption relates to pressure decrease and is the process in production from shale rocks (Li et al. 2014).

In multicomponent mixtures, the extended Langmuir model (ELM) is suggested to describe adsorbed fluids (Ambrose 2011; Leahy-Dios et al. 2011),

$$V_{a,i} = \frac{V_{L,i}\dfrac{p_i}{p_{L,i}}}{1 + \displaystyle\sum_j \frac{p_j}{p_{L,j}}}, \quad \ldots\ldots\ldots\ldots\ldots\ldots\ldots\ldots (3)$$

where $V_{a,i}$ is the adsorption volume of bulk of component i at partial pressure p_i, $V_{L,i}$ is the maximum adsorbed gas volume of bulk for component i, and $p_{L,i}$ represents Langmuir pressure for component i at which the amount of adsorbed gas volume is $V_{L,i}/2$. Parameters $p_{L,i}$ and $V_{L,i}$ are obtained from the pure-component adsorption isotherms. ELM is based on ideal-gas mixture, and the interactions between gas molecules are neglected. Similarly, adsorption is assumed to form a single layer and cannot provide information on the PSD. In **Fig. 2,** we show total fluid in pores for a ternary mixture of C_1, CO_2, and N_2 in activated carbon from Dreisbach et al. (1999). We also show results that are based on density functional theory (DFT) (Li et al. 2014). There is good agreement between DFT and measured data. ELM shows good agreement in methane but significantly underestimates CO_2 and N_2 fluid content. The same as single component Langmuir adsorption, ELM does not include the effect of pore sizes and fluid/fluid interactions. Therefore, it cannot describe capillary condensation or hysteresis.

Fluid Description by EOS. Conventional EOS such as the Peng-Robinson EOS (PR-EOS) are accurate for compositional modeling and description of measured pressure/volume/temperature behavior of reservoir fluids. In general, a cubic EOS can describe phase behavior in porous media characterized by pore sizes larger than 10 nm (Fisher and Israelachvili 1981). In micropores (size < 2 nm), adsorbed properties are strongly affected by fluid/surface interactions depending on chemical composition of porous media. At such scale, the distributions of fluid molecules within the pores are inhomogeneous, and surface adsorption plays a dominant role in fluid-in-place estimation (Li et al. 2014). In small pores, the critical properties are altered (Evans and

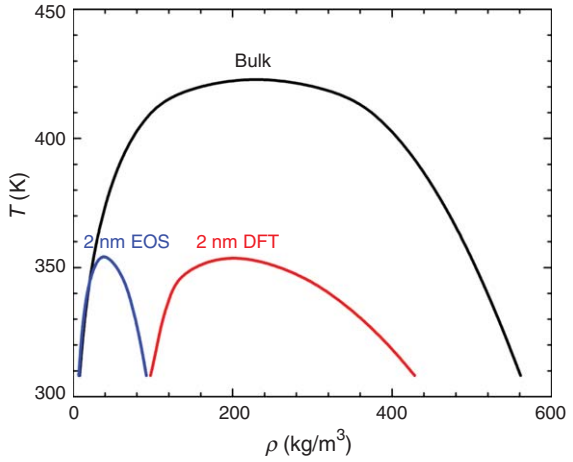

Fig. 3—ρ vs. T diagram of pure nC_4 in 2-nm nanopores from the PR-EOS with shifted critical properties and engineering DFT. Bulk ρ vs. T diagram is from measurements.

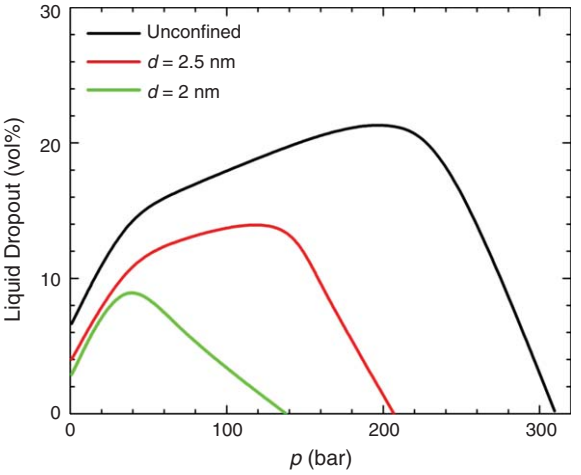

Fig. 4—Liquid dropout for a rich gas condensate in unconfined state and in pores with diameter $d = 2.5$ nm and $d = 2$ nm. Results are from the PR-EOS with shifted critical properties, at 394.26 K.

Tarazona 1984; Evans et al. 1986a, b; Bruno et al. 1987; Balbuena and Gubbins 1993; Morishige et al. 1997; Lev et al. 1999; Zarragoicoechea and Kuz 2004; Kanda et al. 2004; Chen et al. 2008; Singh et al. 2009; Travalloni et al. 2010; Alharthy et al. 2013). The critical temperature of a confined fluid is generally lower than the bulk critical temperature and approaches the bulk value in large pores (Evans and Tarazona 1984; Evans et al. 1986a, b; Balbuena and Gubbins 1993; Morishige et al. 1997; Lev et al. 1999; Reyes 2012). The critical pressure of confined fluid is also reduced in attractive nanopores (Balbuena and Gubbins 1993; Lev et al. 1999). Recently, Didar and Akkutlu (2013) showed that the critical temperature and pressure of methane decrease in carbon nanopores by use of Monte Carlo simulation. Singh et al. (2009) use molecular simulations and show that critical pressure of butane and octane increases in carbon pores larger than 3 nm. In this work, by use of DFT and grand canonical Monte Carlo (GCMC) simulations, we show that both critical temperature and pressure of confined hydrocarbons in carbon nanopores decrease, and as pore size increases, they approach bulk properties.

In recent years, the shifted critical temperature and pressure from Singh et al. (2009) were used in the conventional EOS to generate fluid phase behavior in nanopores (Sapmanee 2011; Devegowda et al. 2012; Alharthy et al. 2013; Jin et al. 2013; Zhang et al. 2013). Note that because pressure in small nanopores varies from point to point, the pressure refers to the reservoir pressure not the pressure in the pores. With the shifted critical temperature and pressure, one can reproduce the saturation pressure of a pure component in nanopores, but densities are significantly underestimated. **Fig. 3** shows the ρ vs. T diagram of pure nC_4 in 2-nm pores from the PR-EOS with the shifted critical properties and the results from the engineering DFT (Li et al. 2014). The shifted critical points are obtained from DFT. The details of calculation of critical points of confined fluids from DFT are given later. For DFT calculations, the nanopores have the same configuration and wettability as in Singh et al. (2009), and densities are the averaged value of the inhomogeneous density distributions within the pores. With the shifted critical temperature and pressure, density predicted from the PR-EOS has a trend similar to that obtained from bulk in gas phase, but it is significantly lower than the bulk in liquid phase. Didar and Akktulu (2013) predict that the average density of methane in carbon nanopores increases, but EOS with shifted critical temperature and pressure show the opposite trend. Significant decrease of liquid density in a nanopore compared with bulk may not be correct. We also use EOS with shifted critical points to investigate the effect of confinement on liquid dropout of a gas condensate with composition from Alharthy et al. (2013). Liquid dropout is defined as the liquid volume divided by the total volume at dewpoint pressure in constant volume depletion. We compute the liquid dropout in unconfined and in confined states. The results are shown in **Fig. 4.** The dewpoint pressure of the rich gas condensate decreases in confinement. Modeling based on bulk phase shows an increase of dewpoint pressure in confinements larger than 10 nm (Firoozabadi 1999; Nojabaei et al. 2013), as we will discuss in detail later. The liquid dropout of the gas condensates predicted from the EOS with shifted critical properties is substantially less than that without confinement. In addition, the use of an EOS with shifted critical properties violates chemical equilibrium between the fluids in the pores and outside fractures and large pores. Therefore, an EOS with shifted critical points cannot be incorporated in a compositional simulator. The assumption of homogeneous density distributions and neglect of surface adsorption in pores less than 3 nm (Alharthy et al. 2013) make the simple application of an EOS unjustified. The limitations in predictions from the Langmuir adsorption isotherms and the cubic EOS motivate this work.

On the basis of experimental evidence, we divide phase behavior in pores greater and less than 10 nm. For pores greater than 10 nm, surface adsorption can be neglected. In both cases, we allow for dissolution in kerogen. We propose a model to combine the free molecules, surface adsorption in micropores, and fluid dissolution in kerogen to estimate fluid-in-place in shale media. We combine the classical thermodynamic approach for phase-behavior description in pores greater than 10 nm and dissolution in kerogen and the statistical thermodynamic approach in pores less than 10 nm. We mostly focus on the use of DFT but also use Monte Carlo simulations to compare critical points from the two methods to resolve the inconsistency in critical pressure.

Species dissolution in kerogen may contribute to fluid-in-place in shale media. There has been no theoretical model on species dissolution in kerogen. In this work, we use a solid solution model (Won 1986) to describe species dissolution in kerogen. Abundant data exist on C_1 and CO_2 sorption in shale. No data have yet been reported on sorption of hydrocarbons heavier than C_1 and mixtures in shale. Our investigation is thus limited to C_1 and CO_2.

The remainder of this article is organized as follows. We first present a brief formulation of our engineering DFT as well as solid solution model. Then, we investigate phase behavior of a gas condensate in retrograde region and gas solubility in water and nC_{10} in pores larger than 10 nm with EOS with curvature effect. We use DFT and GCMC simulations to study the critical point of nC_4 in carbon nanopores. We also study excess sorption in shale small pores by DFT and the solid solution model to account for dissolution and compare computations with experimental data in a number of shale samples. The work ends with Concluding Remarks.

Species	T_c (K)	p_c (bar)	ω	M_w (g/mol)	VSP	ε_g/k_B (K)
C_1	190.56	45.99	0.011	16.04	–0.1533	1178
CO_2	304.14	73.75	0.239	44.01	–0.06225	1760

Table 1—Critical temperature T_c, critical pressure p_c, acentric factor ω, molar weight M_w, volume shift parameter (VSP), and attraction energy parameter ϵ_g for C_1 and CO_2 in the engineering DFT.

Model and Theory

We present the model and theory in pores less than 10 nm and gas dissolution in kerogen. We use DFT to account for inhomogeneous density distributions in small pores and solid solution model to account for gas dissolution in kerogen. The model for pores larger than 10 nm is presented in the Results and Discussion section.

DFT. Within the framework of DFT, one can construct the free energy on the basis of the functionals of heterogeneous molecular distributions. The equilibrium molecular distributions are obtained from the minimization of the grand potential functional, and then macroscopic properties such as sorption amount are readily computed (Li et al. 2014).

We assume that nanopores are connected to a reservoir in which the composition, temperature, and pressure are fixed. The temperature in the nanopore is the same as outside. The volume of the nanopore is fixed. An open system (specified by constant temperature, volume, and chemical potentials) has both energy and mass exchange with the reservoir through an imaginary boundary, and the grand potential is the thermodynamic function of choice (Li et al. 2014). In an open system, the grand potential functional $\Omega[\rho(\mathbf{r})]$ of the system is related to the Helmholtz free-energy functional $F[\rho(\mathbf{r})]$,

$$\Omega[\rho(\mathbf{r})] = F[\rho(\mathbf{r})] + \int \rho(\mathbf{r})[\varphi(\mathbf{r}) - \mu]d\mathbf{r}, \quad \ldots\ldots\ldots\ldots (4)$$

where $d\mathbf{r}$ is the differential volume, $\rho(\mathbf{r})$ is the number density distribution at position $\mathbf{r}$, $\varphi(\mathbf{r})$ is the solid surface external potential at position $\mathbf{r}$, μ is the bulk chemical potential (Li et al. 2009a). At equilibrium, the grand potential functional is minimum,

$$\frac{\delta\Omega}{\delta\rho(\mathbf{r})} = 0. \quad \ldots\ldots\ldots\ldots\ldots\ldots\ldots\ldots\ldots (5)$$

In Eq. 5, the symbol δ represents the functional derivative. With an appropriate expression for excess Helmholtz free-energy functional $F^{ex}[\rho(\mathbf{r})]$ (for details, see Li et al. 2014), minimization of the grand potential functional yields the Euler-Lagrange equation

$$\rho(\mathbf{r}) = \exp\{\beta\mu - \beta\varphi(\mathbf{r}) - \delta\beta F^{\mathrm{ex}}[\rho(\mathbf{r})]/\delta\rho(\mathbf{r})\}, \quad \ldots\ldots (6)$$

where $\beta = 1/(k_B T)$, k_B is the Boltzmann constant, and T is the absolute temperature. In our engineering DFT, the excess Helmholtz free-energy functional is divided into two parts: One part is obtained from the Peng-Robinson equation of state (PR-EOS) (Peng and Robinson 1976; Robinson et al. 1985) by adopting the weighted density approximation (Rosenfeld 1989) to account for physical interactions between fluid molecules; the other part is supplemented by the quadratic density expansion to account for long-range interactions (Ebner et al. 1976; Ebner and Saam 1977) that vanish in the bulk. One can find detailed expressions in Li and Firoozabadi (2009a). Alternatively, one can use the grand canonical Monte Carlo simulations to perform equilibrium calculations, as described in Jin and Firoozabadi (2013).

In this work, we calculate the phase behavior in kerogen as in activated carbon that can be represented by a polydisperse array of carbon slit pores (Ravikovitch et al. 2000; Li et al. 2014). In a slit pore, the density distributions only vary in the z-direction perpendicular to the solid surfaces. The solid surface is assumed to be a planar structureless graphite wall, as in our previous work (Li et al. 2014), and fluid/surface interaction is described by the Steele 10-4-3 potential (Steele 1973)

$$U_{sg}(z) = 2\pi\rho_s\varepsilon_{sg}\sigma_{sg}^2\Delta\left[\frac{2}{5}\left(\frac{\sigma_{sg}}{z}\right)^{10} - \left(\frac{\sigma_{sg}}{z}\right)^4 - \frac{\sigma_{sg}^4}{3\Delta(0.61\Delta + z)^3}\right], \quad \ldots\ldots\ldots\ldots\ldots (7)$$

where $\rho_s = 114$ nm^{-3} is the density of graphite and $\Delta = 0.335$ nm is the interlayer spacing of graphite. ε_{sg} and σ_{sg} are obtained from the Lorentz-Berthelot mixing rules,

$$\varepsilon_{sg} = \sqrt{\varepsilon_s\varepsilon_g}, \quad \ldots\ldots\ldots\ldots\ldots\ldots\ldots\ldots (8)$$

$$\sigma_{sg} = \frac{1}{2}(\sigma_s + \sigma_g). \quad \ldots\ldots\ldots\ldots\ldots\ldots\ldots\ldots (9)$$

In Eqs. 8 and 9, ε_s is the attraction energy parameter of surface molecules, ε_g is the attraction energy parameter of species molecules (Li and Firoozabadi 2009a), $\sigma_s = 0.3345$ nm is the diameter of surface molecules (Olivier 1995), and σ_g is the "molecular diameter" of species calculated from the volume parameter of the PR-EOS (Li and Firoozabadi 2009a). The external potential $\varphi(\mathbf{r})$ in slit pores is given as

$$\varphi(\mathbf{r}) = U_{sg}(z) + U_{sg}(H - z), \quad \ldots\ldots\ldots\ldots\ldots\ldots (10)$$

where H is the apparent size of a slit pore. The inner or effective pore size H_{in} is

$$H_{in} = H - \sigma_s. \quad \ldots\ldots\ldots\ldots\ldots\ldots\ldots\ldots (11)$$

The density distribution in Eq. 6 is solved by the Picard iteration method. The calculation of an isotherm starts at a sufficiently low pressure and ends at a sufficiently high pressure in the adsorption process. At the first pressure in which the initial guess is not available, the bulk density is used for the initialization. The solution of density distributions at other pressures uses the results at the previous pressure as the initial guess. We introduce the volume translation (Jhaveri and Youngren 1988) to correct the equilibrium density distribution calculated from Eq. 6. The PR-EOS parameters are given in **Table 1.** Dimensionless volume shift parameter (VSP) is obtained by fitting the equilibrium liquid density at $T = 0.7T_c$. We use surface attraction parameter $\varepsilon_s/k_B = 20$ K, as given in Li et al. (2014).

Excess sorption per unit inner pore volume (PV) $\rho_{\mathrm{ave,ex}}$ is given as

$$\rho_{\mathrm{ave,ex}} = \frac{\int_0^H [\rho(z) - \rho_b]\mathrm{d}z}{H_{in}}, \quad \ldots\ldots\ldots\ldots\ldots (12)$$

where ρ_b is the bulk density. We assume that shale nanopores are represented by a polydisperse array of carbon-slit pores (Li et al. 2014). This model is also considered to be a good approximation to the organic shale medium (Adesida et al. 2011; Kuila and Prasad 2011). On the basis of the polydisperse carbon-slit-pore model, we characterize the pore structure and predict excess sorption in organic materials by approximate solution of the excess sorption integral

Component	mole (%)	T_c (K)	p_c (bar)	ω	M_w (g/mol)	VSP	$k_{i\text{-}C_1}$	$k_{i\text{-}CO_2}$
C_7	0.178	556.48	26.75	0.294	100.0	0.02473	0.043	0.100
C_8	0.331	574.76	25.24	0.418	114.0	0.04775	0.046	0.100
C_9	0.156	593.07	23.30	0.491	128.0	0.06765	0.048	0.100
C_{10}	0.110	617.07	21.55	0.534	142.0	0.08512	0.050	0.100
C_{11}	0.128	638.24	19.74	0.566	156.0	0.1007	0.052	0.100
C_{12}	0.399	657.29	18.31	0.602	170.0	0.1147	0.055	0.100
C_{13}	1.046	675.70	16.96	0.639	184.0	0.1273	0.057	0.100
C_{14}	1.452	691.48	15.75	0.667	198.0	0.1389	0.059	0.100
C_{15}	1.870	707.29	14.72	0.670	212.0	0.1496	0.062	0.100
C_{16}	1.981	722.96	13.79	0.668	226.0	0.1594	0.064	0.100
C_{17}	2.103	738.12	12.98	0.670	240.0	0.1686	0.066	0.100
C_{18}	2.361	749.81	12.31	0.696	254.0	0.1772	0.068	0.100
C_{19}	2.353	761.50	11.68	0.705	268.0	0.1852	0.071	0.100
C_{20}	2.338	773.18	11.07	0.707	282.0	0.1927	0.073	0.100
C_{21}	2.153	784.87	10.57	0.750	296.0	0.1998	0.075	0.100
C_{22}	2.110	795.31	10.12	0.782	310.0	0.2065	0.078	0.100
C_{23}	1.924	805.43	9.71	0.808	324.0	0.2129	0.080	0.100
C_{24}	1.780	814.77	9.33	0.834	338.0	0.2189	0.082	0.100
C_{25}	1.678	823.52	9.01	0.889	352.0	0.2247	0.084	0.100
C_{26}	1.520	832.27	8.68	0.977	366.0	0.2302	0.086	0.100
C_{27}	1.555	840.70	8.40	1.003	380.0	0.2354	0.088	0.100
C_{28}	1.600	848.98	8.14	1.076	394.0	0.2404	0.090	0.100
C_{29}	1.315	857.26	7.95	1.182	408.0	0.2452	0.092	0.100
Heavy component	53.940	905.81	7.50	1.380	630.0	0.2499	0.094	0.110
Asphaltenes	13.617	1074.00	6.34	1.900	800.0	0.3200	0.096	0.110

Table 2—Description of Athabasca bitumen in the PR-EOS (Varet et al. 2013).

$$\Gamma^a_{\text{ex}}(T,p) = \int \rho_{\text{ave,ex}}(T,p,H_{in})PSD(H_{in})\text{d}H_{in}, \quad \ldots\ldots\ldots (13)$$

where $\Gamma^a_{ex}(T,p)$ is the measured excess sorption in nanopores and *PSD* is the pore-size distribution. We characterize the pore structure of porous media (i.e., solve for the PSD by minimizing the difference between measured and computed Γ^a_{ex} of pure substances). We first generate the data bank of the excess sorption per unit inner PV $\rho_{\text{ave,ex}}(T,p,H_{in})$ with DFT at various pressures and pore sizes. Then, we match the measured excess sorption for given pressures by means of Eq. 13, constructing the PSD on the basis of the least-squares fitting. We assume that the PSD can be readily described by summation of n log-normal distributions (Li et al. 2014),

$$PSD(H_{in}) = \sum_{i=1}^{n} \frac{\alpha_i}{\sqrt{2\pi}\beta_i} \exp\left\{-\frac{[\ln(H_{in}) - \gamma_i]^2}{2{\beta_i}^2}\right\}. \quad \ldots\ldots (14)$$

The $3n$ unknown parameters α_i, β_i and γ_i are determined from the adsorption data of pure substances. Unlike other porous media such as activated carbon (Li et al. 2014), the pore-size distribution in shale media can have multiple peaks (Ross and Bustin 2009). We use $n = 6$ to match the model results with experimental data; $n = 6$ produces good match with measured excess sorption. Pore sizes have a broad range of distributions in shale rocks (Ross and Bustin 2009). Although we assume that surface adsorption in pores larger than 10 nm is small, we construct the adsorption data bank $\rho_{\text{ave,ex}}(T,p,H_{in})$ to 20 nm. As expected, the PSD model is less sensitive to larger pores, and it cannot be used to compute PSD beyond 20 nm.

In shale media, PSD can have a wide range of distributions from less than a few nanometers to micrometers. Mercury intrusion, nitrogen adsorption/desorption isotherm at 77 K, and CO_2 adsorption at 273 K have been used to measure PSD of shale. As we explain later, when pore size is larger than 10 nm, surface adsorption becomes less significant, and excess sorption is negligible.

Solid-Solution Model. The solid-solution model was used to describe wax (Won 1986; Wang et al. 2013a) and asphalthene (Pan and Firoozabadi 1998) precipitations in petroleum fluids. Within the framework of the solid-solution model, a single homogeneous solid solution is in equilibrium with liquid solution or a gas mixture. We assume that solid phase is composed of dissolved species and kerogen. This work is limited to dissolution of single species. We assume no dissolution of kerogen in gas and liquid phases. This is a justified assumption because of negligible vapor pressure of kerogen.

We assume a single, homogeneous solid solution S to be in equilibrium with a pure component in a gas or in liquid state; let us assume the gas state G. At equilibrium, the fugacity of gas component g in the solid phase f^S_g is equal to $f^G_{g,0}$ in the gas phase at given pressure p and temperature T,

$$f^S_g(\mathbf{x}^S,p,T) = f^G_{g,0}(p,T), \quad \ldots\ldots\ldots\ldots\ldots\ldots (15)$$

where $\mathbf{x}^S$ is the composition in the solid solution. In this work, we assume that kerogen behaves similarly to bitumen. One can use the PR-EOS to describe the dissolution of a single component gas or liquid in a bitumen liquid (Varet et al. 2013). The comparison between the PR-EOS calculations and experimental data is presented in Appendix A. The composition, parameters of pseudocomponents in the PR-EOS, and binary-interaction coefficients with C_1 and CO_2 are shown in **Table 2.**

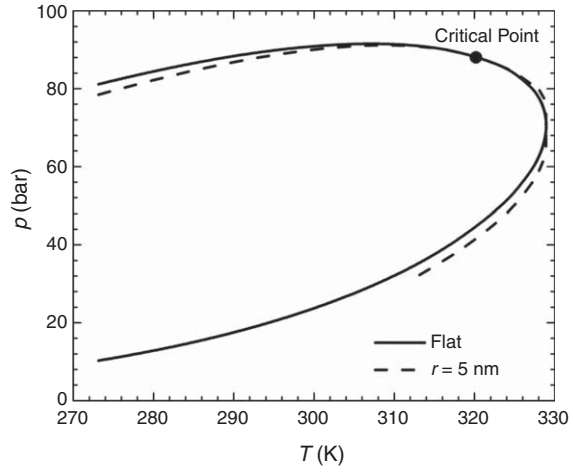

Fig. 5—*p* vs. *T* diagram of equimolar mixtures of C_1 and C_3 for curved ($r = 5$ nm) and flat interface from the PR-EOS.

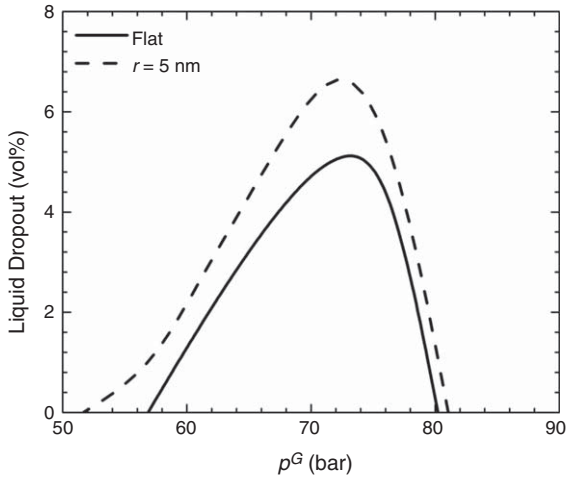

Fig. 6—Liquid dropout of equimolar mixtures of C_1 and C_3 for curved ($r = 5$ nm) and flat interface from the PR-EOS at $T = 327.15$ K.

Within the framework of the solid-solution model,

$$f_g^S(\mathbf{x}^S, p, T) = \gamma_g^S(\mathbf{x}^S, p, T) x_g^S f_{g,0}^S(p, T), \quad \ldots\ldots\ldots\ldots (16)$$

in which γ_g^S is the activity coefficient of gas component, x_g^S is the mole fraction of gas component, and $f_{g,0}^S$ is the fugacity of pure gas component all in solid phase. γ_g^S represents the nonideality because of the interactions between gas and kerogen molecules in solid phase. In this work, we use solubility parameters (Won 1986; Wang et al. 2013a) to estimate γ_g^S. The fugacities of pure gas component in the solid and gas states are related through (Firoozabadi 1999)

$$f_{g,0}^S(p, T) = f_{g,0}^G(p, T) \exp\left[\frac{\mu_{g,0}^S(p, T) - \mu_{g,0}^G(p, T)}{RT}\right], \quad \ldots\ldots (17)$$

in which $\mu_{g,0}^G(p, T)$ is the chemical potential of pure gas component at pressure p and temperature T, and $\mu_{g,0}^S(p, T)$ is the chemical potential of the pure superheated solid at the same temperature and pressure. Details of fugacity calculation of pure superheated solid C_1 and solid CO_2 are given in Appendix B. The calculation of activity coefficients in solid solution is presented in Appendix C.

We use the symbol Γ_{ex}^s to represent the gas dissolution in kerogen,

$$\Gamma_{\text{ex}}^s(p, T) = \frac{x_g^S M_g}{\sum_{i \neq g} x_i^S M_i}, \quad \ldots\ldots\ldots\ldots\ldots\ldots (18)$$

where M_i is the molecular weight of component i. The total excess sorption Γ_{ex} is expressed by

$$\Gamma_{\text{ex}} = \Gamma_{\text{ex}}^a + \Gamma_{\text{ex}}^s. \quad \ldots\ldots\ldots\ldots\ldots\ldots\ldots (19)$$

Note that when there is no dissolution, there is only excess (ad)sorption onto the solid surface. In this work, we use the composition of Athabasca bitumen from Varet et al. (2013) to model kerogen.

Results and Discussion

Effect of Curvature on Phase Behavior in Pores Larger Than 10 nm. In pores larger than 10 nm, surface adsorption can be neglected; the density distribution within a pore is homogeneous except close to the walls. The effect of curvature on phase behavior is well-established when pore size is more than 10 nm (Fisher and Israelachvili 1981). The Kelvin equation provides the curvature effect in single components when the gas phase is ideal and the liquid phase is incompressible. When the liquid phase wets the substrate, curvature lowers the saturation pressure. In a multicomponent system, curvature can result in an increase or a decrease of saturation pressure (Firoozabadi 1999). A number of recent papers describe the effect of curvature on saturation pressure and phase equilibrium of hydrocarbon mixtures (Du and Chu 2012; Nojabaei et al. 2013; Wang et al. 2013b). In this work, we address two important aspects: (1) retrograde condensation and (2) solubility of methane and CO_2 in water and in *n*-decane caused by interface curvature.

We use the following expressions to perform our computations,

$$P_c = p^G - p^L = 2\sigma/r, \quad \ldots\ldots\ldots\ldots\ldots\ldots (20)$$

$$\mu_i^G = \mu_i^L, \quad \ldots\ldots\ldots\ldots\ldots\ldots\ldots\ldots (21)$$

where P_c is the capillary pressure, p^G is the gas phase pressure, p^L is the liquid phase pressure, σ is the surface tension, and μ_i^G and μ_i^L are chemical potentials of component i in gas and liquid phases, respectively. One can use the Weinaug-Katz model (Weinaug and Katz 1943) to calculate σ,

$$\sigma^{1/4} = \sum_{i=1}^{c} P_i \left[y_i(d^G/M^G) - x_i(d^L/M^L)\right], \quad \ldots\ldots\ldots (22)$$

in which x_i and y_i are the mole fractions of component i in the liquid and gas phases; d^L and d^G are mass densities in the liquid and gas phases, respectively; M^L and M^G are molecular weight in the liquid and gas phases, respectively; and P_i is the parachor of component i and c is the number of components.

Fig. 5 shows the p vs. T diagram of equimolar mixtures of C_1 and C_3 for curved (pore radius 5 nm) and flat interfaces. The PR-EOS is used to describe phase diagram. The bubblepoint pressure decreases, the retrograde (upper) dewpoint pressure increases, and regular (lower) dewpoint pressure decreases because of the curvature effect. The decrease of bubblepoint pressure in liquid-rich shale reservoir fluids was reported by Du and Chu (2012) and Alharthy et al. (2013). The interface curvature also affects the liquid dropout of the C_1/C_3 mixture, as shown in **Fig. 6.** Liquid forms at a higher pressure (increase in upper dewpoint pressure); there is increase in retrograde condensation throughout the pressure decrease, and there is a substantial decrease of the lower dewpoint pressure, all from the curvature effect. Trebin and Zadora (1968) present experimental data that show that the tight pores of a porous medium decrease the liquid content of the produced fluid of gas condensates. In other words, porous media result in an increase of liquid dropout. The measurements are in support of our computations. **Fig. 7** presents liquid dropout of a

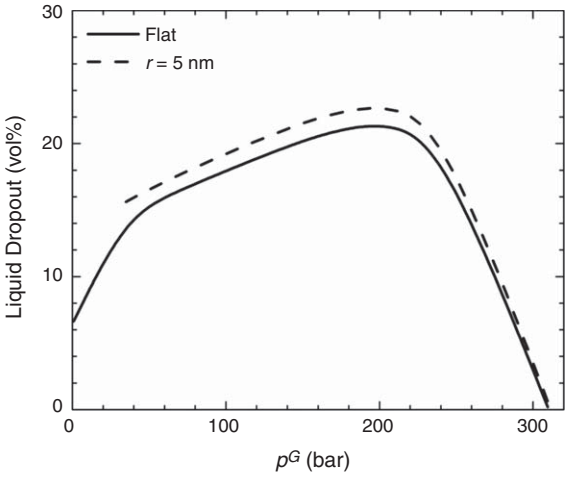

Fig. 7—Liquid dropout of rich gas condensate for curved ($r = 5$ nm) and flat interface from the PR-EOS at $T = 394.26$.

rich gas condensate and the effect of curved interface ($r = 5$ nm). Composition is taken from Alharthy et al. (2013). Because the gas and liquid phase pressures are different (resulting from capillarity), results are presented in terms of gas-phase pressure. The liquid dropout caused by the curved interface cannot be extended to $p^G = 1$ bar; we find that, at low pressure, the fluid mixture is in a single phase. The upper dewpoint pressure increases approximately 1 bar because the interfacial tension is small at a pressure of approximately 310 bar. Fig. 7 clearly indicates an increase in liquid dropout similar to the binary C_1/C_3 mixture caused by the curvature effect. Note that such a behavior is opposite to predictions from the EOS with shifted critical properties shown in Fig. 4. Perhaps one should not use an EOS for nonhomogeneous fluid distribution with shifted critical pressure and temperature.

Next, we present results from the effect of curvature on gas solubility in water. We assume that water is the wetting phase and gas is the nonwetting phase. This assumption may not be valid in kerogen pores. In **Fig. 8,** we present the effect of interface curvature on solubility of C_1 and CO_2 in water at $T = 350$ K. We use the cubic-plus-association EOS (CPA-EOS) (Li and Firoozabadi 2009b) to describe water and its interaction with nonpolar species. The CPA-EOS is accurate for description of water/CO_2 and water/hydrocarbon mixtures. Gas-phase pressure is fixed at $p^G = 500$ bar, and liquid-phase pressure p^L varies with curvature. The surface tensions of C_1/H_2O and CO_2/H_2O mixtures are 44 mN/m (Firoozabadi 1999) and 25 mN/m (Espinoza and Santamarina 2010), respectively. We calculate the effect of curvature to radius $r = 5$ nm. As pore size decreases, solubility of methane and CO_2 increases. The increases in solubility of methane and CO_2 in water are up to 20 to 30%, respectively. Results when gas is the wetting show a decrease in solubility with curvatures increase (not shown for the sake of brevity). Campos et al. (2009) predict that the density of dissolved methane in water in 10 nm pores is 117×10^{-3} g/cm^{3}at pressure of 276 bar and temperature of 353.15 K by a simple analytical method. For the same pressure and temperature, density of dissolved methane in bulk water and density of pure methane are 1.76×10^{-3} g/cm^3 and 149×10^{-3} g/cm^3, respectively. There is a two-order-of-magnitude increase in methane solubility in water in a 10-nm pore. Campos et al. (2009) state "methane stored as dissolved gas in brine for a 1000 nm^3 pore volume (10-nm pore) is comparable to the amount of methane that would be stored in the pore if it was just filled with gas at the same reservoir conditions." They use what one can describe as the limit of stability of methane in water to describe the solubility in nanopores. The limit of stability of methane in water can be orders of magnitude larger than the equilibrium solubility (Jiménez-Ángeles and Firoozabadi 2014). Equality of chemical potentials or chemical equilibrium is not considered by Campos et al. (2009).

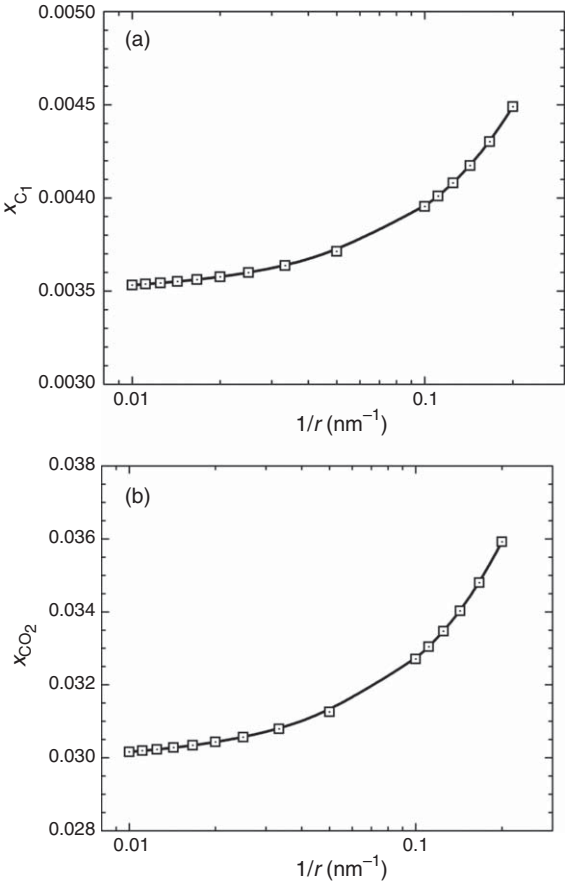

Fig. 8—Solubility of (a) C_1 (b) CO_2 in water vs. interface curvature ($1/r$) at $T = 350$ K and gas-phase pressure $p^G = 500$ bar.

We also investigate the effect of curvature on equilibrium for gas solubility in *n*-decane (nC_{10}). We assume that nC_{10} is the wetting phase, and gas is the nonwetting phase. **Fig. 9** depicts the effect of interface curvature on solubility of C_1 and CO_2 in nC_{10} at $T = 366.48$ K and $T = 344.30$ K, respectively. We use the PR-EOS to describe bulk phases. Gas-phase pressure is fixed at $p^G = 100$ bar, and liquid-phase pressure p^L varies with curvature. The surface tensions of C_1-nC_{10} and CO_2-nC_{10} mixtures are 9.22 mN/m (Amin and Smith 1998) and 3.05 mN/m (Nagarajan and Robinson 1986) at the corresponding conditions, respectively. Similar to solubility in water, solubility of C_1 and CO_2 increases with curvature. The increase in solubility is up to 10%.

Critical Point of Confined Hydrocarbons in Carbon Nanopores. In small nanopores, caused by strong fluid/surface interactions, the properties of confined fluids are different from bulk, and critical properties are shifted. Singh et al. (2009) report that critical temperatures of confined *n*-butane and *n*-octane in graphene nanopores decrease, but critical pressure and saturation pressure of confined fluids are higher than bulk when pores are larger than 3 nm. Because graphene is oil-wet, the saturation pressures and critical pressures should decrease. We use engineering DFT and GCMC method to investigate the critical pressure and temperature of nC_4 in nanopores.

In engineering DFT, nC_4 is considered as a structureless molecule. In GCMC simulations, we explicitly consider molecular configurations and intermolecular interactions. We use the united atom model (Martin and Siepmann 1998) to simulate nC_4 molecules. Nonbonded site/site interactions are described by the modified Buckingham exponential intermolecular potential (Errington and Panagiotopoulos 1999), for which the pairwise interaction potential $U(r)$ is presented as

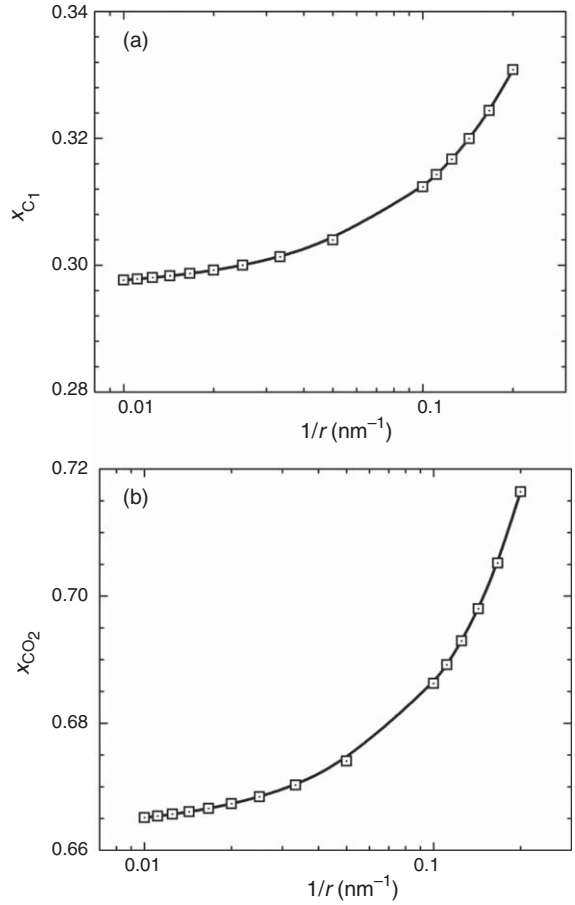

Fig. 9—Solubility of (a) C_1 at $T = 366.48$ K (b) CO_2 at $T = 344.30$ K in nC_{10} vs. interface curvature (1/r) and gas-phase pressure $p^G = 100$ bar.

$$U(r) = \left(\frac{\varepsilon}{1-\frac{6}{\alpha}}\left\{\frac{6}{\alpha}\exp\left[\alpha\left(1-\frac{r}{r_m}\right)\right]-\left(\frac{r_m}{r}\right)^6\right\}\right), \quad r > r_{\max}$$
$$= \infty, \quad r < r_{\max}, \quad \ldots\ldots\ldots\ldots\ldots\ldots (23)$$

in which ε, r_m, and α are adjustable parameters. The variable r_m is the radial distance at which $U(r)$ reaches a minimum, and the cutoff distance $r_{\max}$ represents the smallest radial distance for which $dU(r)/dr = 0$ (Singh et al. 2009). The parameters ε and α are 129.63 K and 16, respectively, for the methyl group (-CH_3), and 73.5 K and 22, respectively, for the methylene group (-CH_2-). Unlike interactions are computed with the standard Lorentz-Berthelot mixing rules.

The bond lengths CH_3-CH_2 and CH_2-CH_2 are 0.1687 and 0.1535 nm, respectively. The bond-bending potential is given as (van der Ploeg and Berendsen 1982)

$$U_{\text{bend}}(\theta) = \frac{K_\theta}{2}(\theta - \theta_{eq})^2, \quad \ldots\ldots\ldots\ldots\ldots\ldots (24)$$

where $K_\theta = 62500$ K/rad^2 and $\theta_{eq} = 114°$. Torsion energy is given as (Smit et al. 1995)

$$U_{tor}(\varphi) = V_0 + \frac{V_1}{2}(1+\cos\varphi) + \frac{V_2}{2}(1-\cos 2\varphi) + \frac{V_3}{2}(1+\cos 3\varphi), \quad \ldots\ldots\ldots\ldots\ldots\ldots (25)$$

where $V_0 = 0$, $V_1 = 355.03$ K, $V_2 = -68.19$ K, and $V_3 = 791.32$ K.

In this subsection, we assume that pores are of slit geometry with smooth and structureless surfaces. For hydrocarbon molecules, the fluid/wall interactions U_{wf} are modeled by the 9-3 Steele potential (Steele 1973)

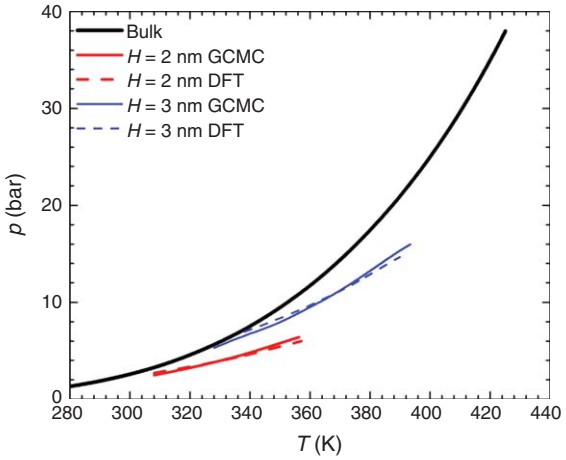

Fig. 10—p vs. T diagram of bulk nC_4 and confined nC_4 in graphene nanopores from DFT and GCMC.

$$U_{wf}(z) = \frac{2}{3}\pi\rho_w\varepsilon_{wf}\sigma_{wf}^3\left\{\frac{2}{15}\left(\frac{\sigma_{wf}}{z}\right)^9 - \left(\frac{\sigma_{wf}}{z}\right)^3\right\}, \quad \ldots\ldots (26)$$

where z is the distance of the fluid particle from the wall and ρ_w, ε_{wf}, and σ_{wf} are the parameters of the Steele potential. $\sigma_{wf} = (\sigma_w + \sigma_i)/2$, where σ_w is the diameter of the wall atom and σ_i is diameter of a hydrocarbon atom. Potential parameters for graphene surfaces are $\rho_w = 33$ nm^{-3}, $\varepsilon_{wf} = 84$ K, and $\sigma_w = 0.392$ nm, respectively (Singh et al. 2009). The diameters of hydrocarbon atoms are 0.3679 nm for the methyl group (-CH_3) and 0.400 nm for the methylene group (-CH_2-), respectively. In each MC cycle, a trial random displacement and rotation is applied to all nC_4 molecules, and one nC_4 molecule is randomly removed from or created at equal probability depending on the chemical potential of nC_4. We use a configurational-biased MC algorithm to insert and remove nC_4 molecules (Hensen et al. 2001). The chemical potential is obtained from Widom's particle-insertion method (Widom 1963) for NVT (constant number of molecules, volume and temperature) MC simulation of bulk nC_4.

We use both DFT and GCMC to compare with the results from Singh et al. (2009). For DFT, the external potential for two CH_3/wall and two CH_2/wall interactions are modeled. To determine the critical temperature and pressure of nC_4 in nanopores, we first obtain saturation pressure of confined nC_4 for a given temperature and pore size. The capillary condensation pressure represents the saturation pressure of confined fluids. At capillary condensation pressure, there is a sudden jump in average density in nanopores through adsorption isotherm (Li and Foroozabadi 2014). One can find the details of the calculation of capillary condensation pressure in Li et al. (2014). We also calculate the average densities in nanopores of vapor-like phase ρ_v and liquid-like phase ρ_l at saturation pressure. The vapor/liquid critical temperature is obtained by fitting ρ_v and ρ_l at saturation pressure to the law of the rectilinear diameter (Rowlinson and Swinton 1982) and the scaling law for density (Rowlinson and Widom 1982)

$$\rho_l - \rho_v = B\left(1-\frac{T}{T_c}\right)^\beta, \quad \ldots\ldots\ldots\ldots\ldots\ldots (27)$$

$$(\rho_l + \rho_v)/2 = \rho_c + A\left(1-\frac{T}{T_c}\right)^\beta, \quad \ldots\ldots\ldots\ldots\ldots\ldots (28)$$

in which A and B are adjustable parameters, ρ_c is the critical density, T_c is the critical temperature, and β is the critical exponent. The critical pressure p_c is calculated by fitting the saturation pressure (p_s) data to the following expression (Singh et al. 2009)

$$\ln p_s = A' - \frac{B'}{T}, \quad \ldots\ldots\ldots\ldots\ldots\ldots (29)$$

	DFT		GCMC		Singh et al. (2009)	
H (nm)	T_c (K)	p_c (bar)	T_c (K)	p_c (bar)	T_c (K)	p_c (bar)
2	357.11	5.99	356.33	6.41	362.14	28.04
3	392.60	15.07	393.43	15.98	387.33	39.15

Table 3—Critical points of confined nC$_4$ from our DFT and GCMC calculations and from Singh et al. (2009).

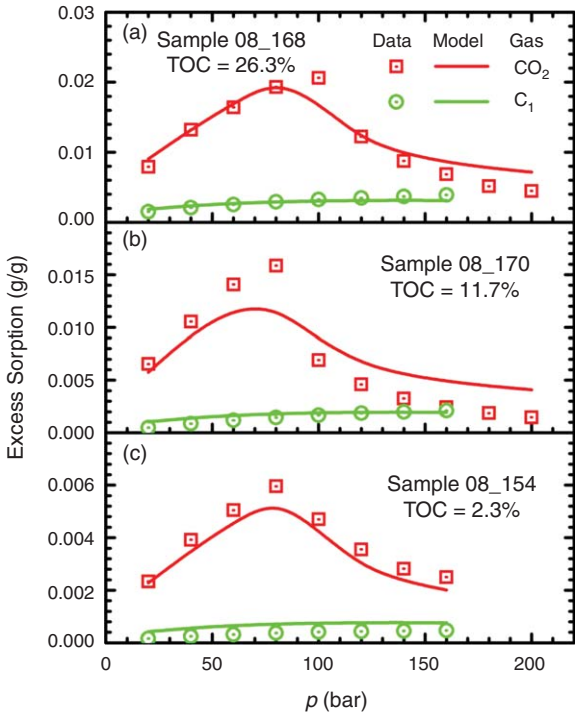

Fig. 11—Excess sorption of C_1 and CO_2 in three different Irati shale samples at 318.15 K from the model and experimental data (Weniger et al. 2010).

where A' and B' are adjustable parameters. The critical pressure p_c is obtained when $T = T_c$.

Fig. 10 presents the p vs. T diagram of confined nC$_4$ in graphene nanopores with different pore sizes from DFT and GCMC. The agreement between DFT and GCMC is very good. The calculated critical points from DFT and GCMC are presented in **Table 3.** For comparison, we also present the critical point from Singh et al. (2009); critical temperature agrees well with our DFT and GCMC, but significantly overestimates the critical pressure. Our result indicates that both critical temperature and critical pressure of confined nC$_4$ decrease, and as pore size increases, they approach bulk values. Critical temperature and pressure of confined nC$_8$ from DFT and GCMC show similar behavior (not shown). In hydrocarbon-wet nanopores, caused by surface attraction, capillary condensation occurs at a pressure lower than the bulk saturation pressure (Li et al. 2014). On the other hand, Singh et al. (2009) predict that saturation pressure and critical pressure of confined fluids increase when $H \geq 3$ nm. As pore size increases, the correlation between two walls becomes less significant; thus, the properties of confined fluids approach the bulk. However, Singh et al. (2009) predict that critical pressures of confined fluids do not approach the bulk as pore size increases.

Excess Sorption in Shale. As we discussed previously, in pores larger than 10 nm, surface adsorption can be neglected. However, in pores less than 10 nm, fluid-surface interactions are strong, and density distributions are inhomogeneous. Fluids may dissolve in kerogen to further increase fluid-in-place.

In this section, we compare measured excess sorption data of C_1 and CO_2 in shale media to the model results. For most samples, total fluid-in-place is not available. We use DFT for predictions in small pores and the solid-solution model to describe dissolution in kerogen. We assume that kerogen has the same chemical composition as Athabasca bitumen (Varet et al. 2013). As a result, gas dissolution only correlates with total organic carbon (TOC). Shales contain inorganic and organic materials. Clay minerals as part of inorganic matter have nanopores and mesopores that can house the fluids (Jin and Firoozabadi 2013). However, many shale reservoirs (Ross and Bustin 2009; Weniger et al. 2010) also have water or are moisture-saturated that blocks the pores in hydrophilic clays (Ji et al. 2012; Jin and Firoozabadi 2014). Some of the fluids used in this work are moisture-saturated that result in a small amount of gas in clay minerals. We do not consider gas adsorption in clay minerals. There is much data on C_1 and CO_2 excess sorption in shale media, but to the best of our knowledge, no measurement was conducted on heavier hydrocarbons and mixtures. As stated previously, mainly excess sorption data are reported in different shale samples.

Fig. 11 presents our model results and experimental data (Weniger et al. 2010) of C_1 and CO_2 excess sorption in three different Irati Shale samples from Brazil. The TOC of each sample is listed in **Table 4.** Generally, excess sorption increases with TOC. The overall agreement between our model results and experimental data is good. For C_1, the excess sorption increases with pressure and reaches a plateau. However, for CO_2, as pressure increases, the excess sorption increases then decreases. At low pressure, surface sorption is dominant. This is because the attraction between pore walls and CO_2 molecules is stronger than that between pore walls and C_1 molecules. As a result, the pores are quickly saturated by CO_2. An increase then a decrease of

Reference	Sample	TOC (wt%)
Weniger et al. (2010)	08_154	26.3
	08_168	11.7
	08_170	2.3
Heller and Zoback (2014)	Barnett 31	5.3
	Eagle Ford 127	1.8
	Marcellus	1.2
	Montney	2.0
Vermylen (2011)	19HVab	3.4
	22Vab	3.6
	26Vab	4.0
	31Vcde	5.7
Zhang et al. (2012)	Woodford (kerogen)	69.6
	Green River (kerogen)	63.9

Table 4—TOC of different shale rocks.

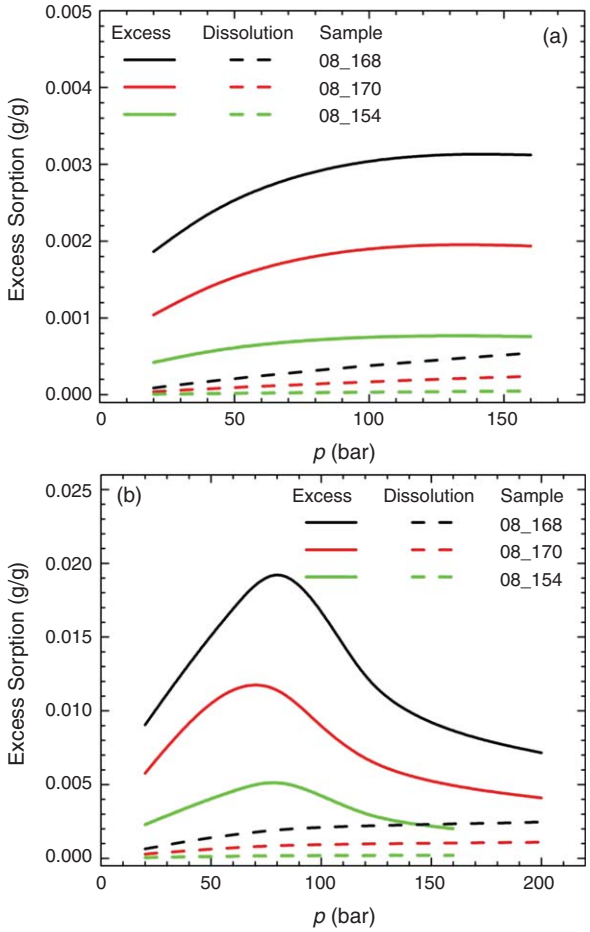

Fig. 12—Excess sorption and dissolution of (a) C_1 (b) CO_2 in three different Irati shale samples from the model.

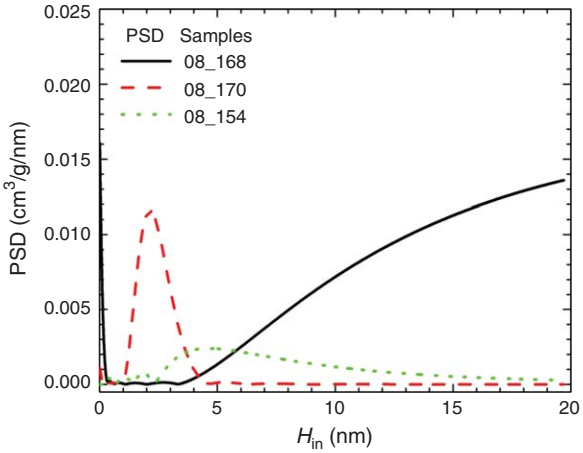

Fig. 13—PSDs of Irati-Shale samples.

excess sorption of CO_2 with pressure was observed in the Sulcis dry coals (Ottiger et al. 2008). The difference between calculated and measured excess sorption of CO_2 may be caused by a charge effect that we do not include in our DFT calculations. Kerogen is different from graphene, which is composed of pure carbon atoms and does not have partial charge on surface atoms. Kerogen has hydrogen, oxygen, nitrogen, and sulfur atoms and functional groups on the surface. Electrostatic interactions between CO_2 and functional groups may increase adsorption (Liu and Wilcox 2012) in heterogeneous carbon nanopores. In **Fig. 12,** we show the calculated excess sorption Γ_{ex} and dissolution Γ^s_{ex} of C_1 and CO_2 in the three shale samples. Note that excess sorption Γ_{ex} includes dissolution Γ^s_{ex}. The difference between these two is a measure of physical surface adsorption onto the surfaces. Unlike excess sorption, dissolution increases with pressure and TOC. At high pressure and high TOC, surface adsorption is still significant for C_1, but for CO_2, dissolution in kerogen is approximately 30% of the excess sorption, indicating that gas dissolution in kerogen may significantly contribute to fluid-in-place. In Fig. 12, the contribution from gas dissolution to the excess sorption is approximately 7% for C_1 and 9% for CO_2 at 45 bar. Etminan et al. (2014) report that methane dissolution in total fluids is approximately 20% at the same pressure. The difference may be because crushed samples are used in Weniger et al. (2010), whereas Etminan et al. (2014) measure dissolution in an uncrushed shale plug. The properties of kerogen may not be properly represented with chemical composition of Athabasca bitumen. In future, when kerogen chemical analysis, pore-size distribution (PSD), and more data become available, we can further advance our model. In **Fig. 13,** we present the PSD computed from the excess sorption data. In contrast to activated carbons (Li et al. 2014), PSDs of shale samples have a broad distribution. Shale may have a significant amount of pores approximately 5 nm and larger than 10 nm, indicating wide distributions in mesopores. Note that our calculated excess sorption becomes fairly insensitive to pores greater than 10 nm. Our model cannot predict PSD when pores are greater than 10 nm, and 20 nm is beyond the range of the adsorption model. Activated carbons may have a majority of pores in less than a 2-nm range (Li et al. 2014). Next, we present excess sorption of shale samples from four different shale reservoirs in the US.

Fig. 14 depicts excess sorption of C_1 and CO_2 from our model and experimental data (Heller and Zoback 2014) at 313.15 K. In contrast to two of the aforementioned shale samples, the TOC of these four shale samples is relatively low. The agreement between our model results and experimental data is good. Despite relatively low TOC, excess sorption of C_1 and CO_2 in Marcellus (TOC 1.2 wt%) and Montney (TOC 2.0 wt%) shales is comparable to that of Barnett shale (TOC 5.3 wt%). The data reveal that at low TOC, surface adsorption may play a key role. **Fig. 15** indicates that excess sorption Γ_{ex} is much higher than dissolution Γ^s_{ex} of C_1 and CO_2, especially for low TOC as expected. **Fig. 16** presents the computed PSD with a number of peaks; most of the pores are less than 10 nm. These results are in contrast to PSD of two of shale samples in Fig. 14. In the following, we show results for four other samples, all from the Barnett shale.

Our model results and experimental data from Vermylen (2011) are shown in **Fig. 17** for excess sorption of C_1 and CO_2 at 298.15 K. At this temperature, C_1 has a Langmuir adsorption behavior, and CO_2 has a Brunauer-Emmett-Teller (BET) adsorption behavior (Vermylen 2011). In BET theory, molecules can form multilayer adsorption, and adsorption continuously increases with pressure. As pressure increases, C_1 excess sorption reaches a plateau, but CO_2 excess sorption continuously increases. Our model faithfully captures such difference in C_1 and CO_2 excess sorption. Because we do not consider charge effect in our DFT calculations, there are differences between our model results and measured CO_2 excess sorption. We show the corresponding PSD in **Fig. 18.** In these Barnett Shale samples, the majority of pores are greater than 2 nm. In the final comparison, we investigate the effect of temperature and high kerogen content on methane excess sorption.

Zhang et al. (2012) provide C_1 excess-sorption data in isolated kerogen of different kerogen-rich shale samples at various temperatures. We show both data and our model results in **Fig. 19.** The TOCs of the isolated kerogen samples are approximately 70% (Table 4). At different temperatures, our model shows agreement with experimental data. Our results are in agreement with data at lower temperatures ($T = 308.55$ K). As temperature increases, C_1 excess sorption and dissolution in kerogen decrease. The excess sorption Γ_{ex} and dissolution Γ^s_{ex} of C_1 are shown in **Fig. 20.** At high pressure, the contribution from C_1 dissolution in kerogen to excess sorption can be as high as 20%. The corresponding PSDs are shown in **Fig. 21,** which indicates that pores mainly distribute in $H_{in} \geq 5$ nm range.

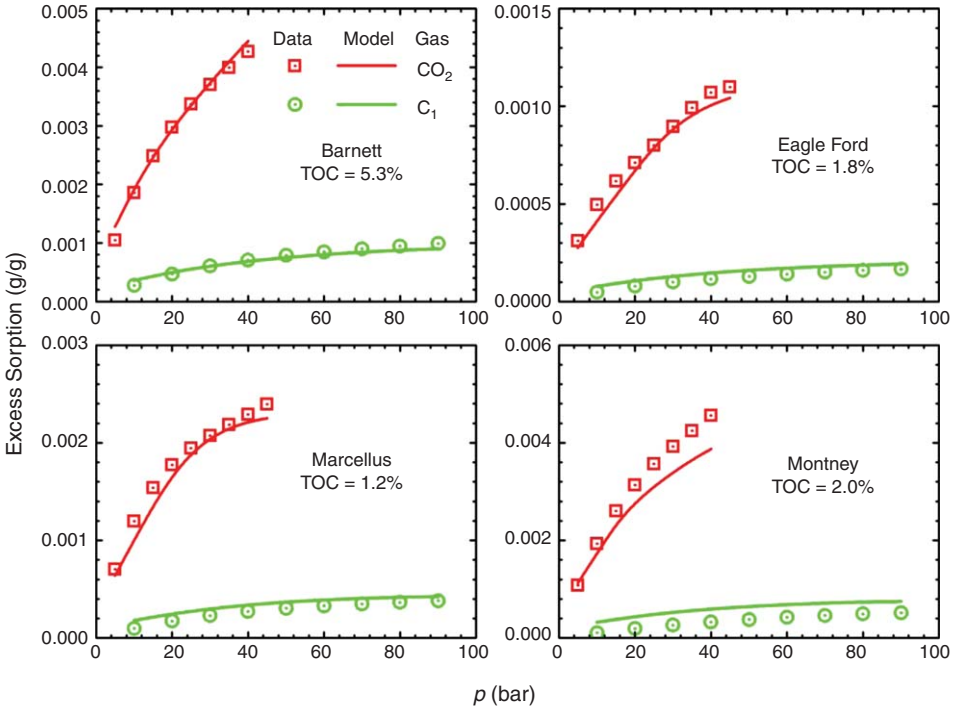

Fig. 14—Excess sorption of C_1 and CO_2 in four shale samples at 313.15 K from the model and experimental data (Heller and Zoback 2014).

Concluding Remarks

Phase behavior in shale media is different from that in conventional rocks and even in tight rocks. Conventional approaches such as the Langmuir adsorption isotherm and equations of state (EOS) with shifted critical properties have major drawbacks. The problem is new and requires reporting of pore-size distribution and chemical analysis of the kerogen and the amount of the kerogen. In this work, we integrate different mechanisms of phase behavior of fluids in shale media and their effects on fluid-in-place. Specific findings from this work are:

- In pores larger than 10 nm (to, say, less than 100 nm), where bulk-phase description applies, interface curvature affects saturation pressure and composition of the phases. There may be an increase in upper dewpoint pressure and a decrease in bubblepoint and lower dewpoint pressure. There is also an increase in liquid dropout as a result of interface curvature. These aspects are in agreement with measured data in inorganic matter. The curvature effect results in a modest increase of gas solubility in the aqueous phase when we assume that water is the wetting phase. There is also a modest increase in solubility in liquid hydrocarbons. A two-order-of-magnitude increase in solubility in water resulting from curvature suggested by some authors cannot be supported on the basis of bulk-phase thermodynamic equilibrium.

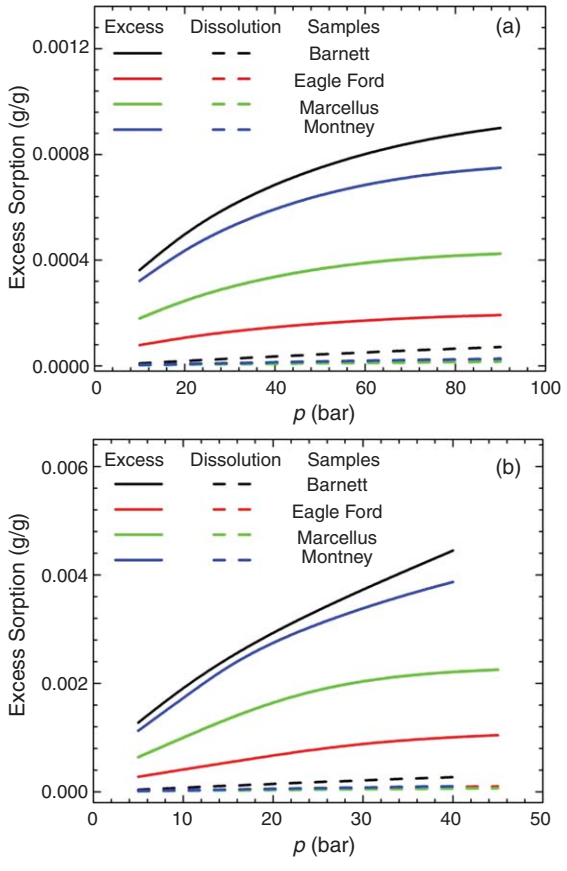

Fig. 15—Excess sorption and dissolution of (a) C_1 (b) CO_2 in four shale samples from the model.

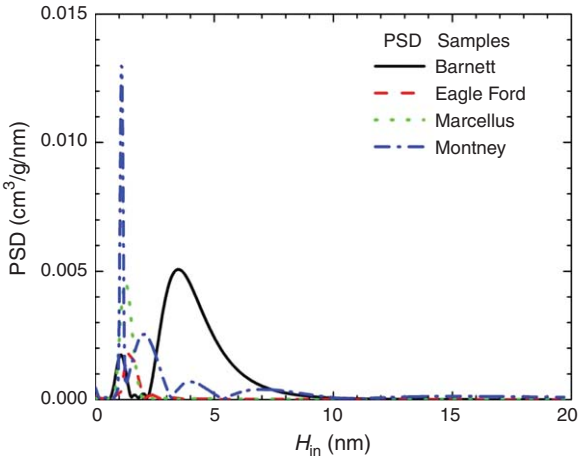

Fig. 16—PSDs of four shale samples.

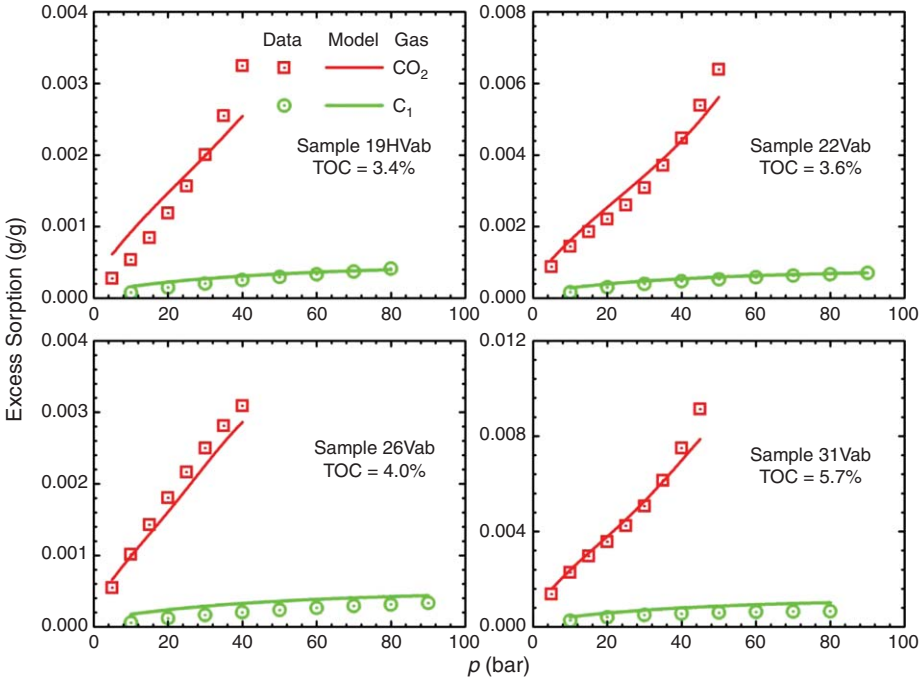

Fig. 17—Excess sorption of C_1 and CO_2 in shale samples at 298.15 K from our model and experimental data (Vermylen 2011).

- In pores less than 10 nm, surface adsorption becomes significant, and fluids have an inhomogeneous density distribution caused by strong fluid/surface interactions. As a result, critical properties are shifted. Use of a cubic EOS with shifted critical properties significantly underestimates the average liquid density in pores. The adjusted EOS predicts a significant decrease in liquid drop in the retrograde region and a decrease in upper dewpoint pressure. These results are not consistent with low recovery from shale reservoirs. There is no basis to use an EOS in nanopores. We propose the use of molecular modeling such as density functional theory and Monte Carlo simulations. As we learn more about kerogen composition and partial charge of heteroatoms, one may need to account for charge effect in calculations for water and CO_2. The saturation pressure and critical properties of light normal alkanes decrease in graphene nanopores. As pore size increases, critical pressures and temperatures approach the bulk value. Our results do not confirm results of critical pressure increase reported in the literature.
- Species dissolution in kerogen may provide an additional fluid-in-place mechanism in shale media. We have proposed a model to compute species dissolution in the solid solution. Activity coefficient of the species in kerogen is a key element of our proposed model. In some kerogen-rich shale samples, dissolution of CO_2 in kerogen is estimated to be as high as 30% of the excess sorption.

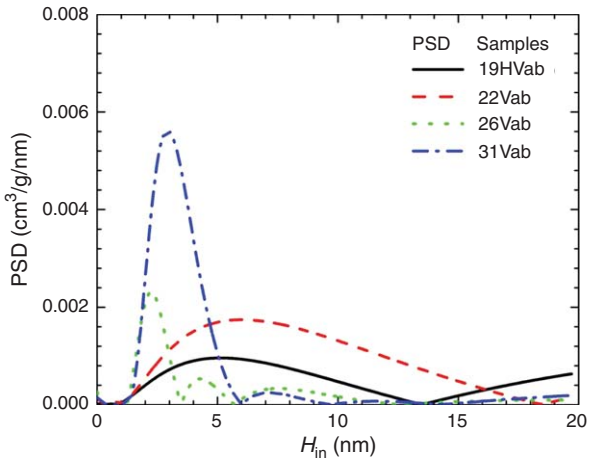

Fig. 18—PSDs of the Barnett shale samples.

Nomenclature

c = number of components
$C_{g,p}$ = heat capacity of gas component
d^G = mass density of the gas phase
d^L = mass density of the liquid phase

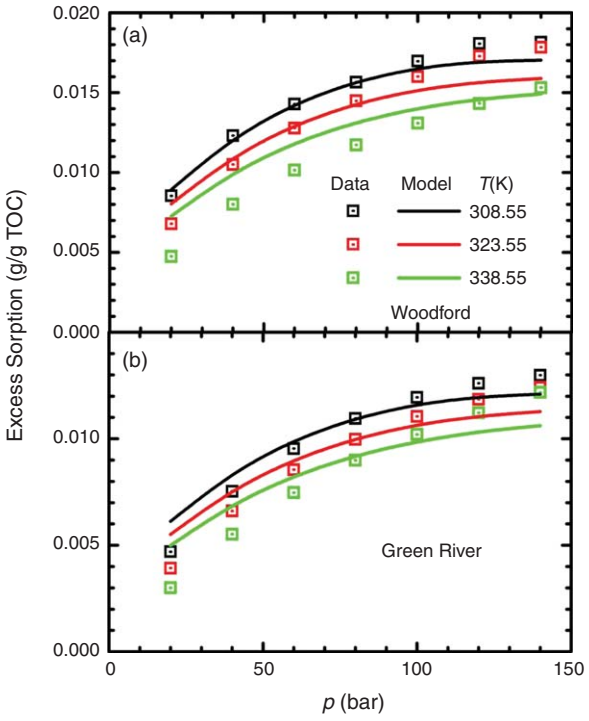

Fig. 19—Excess sorption of C_1 in isolated kerogen from shale samples at different temperatures from our model and experimental data (Zhang et al. 2012).

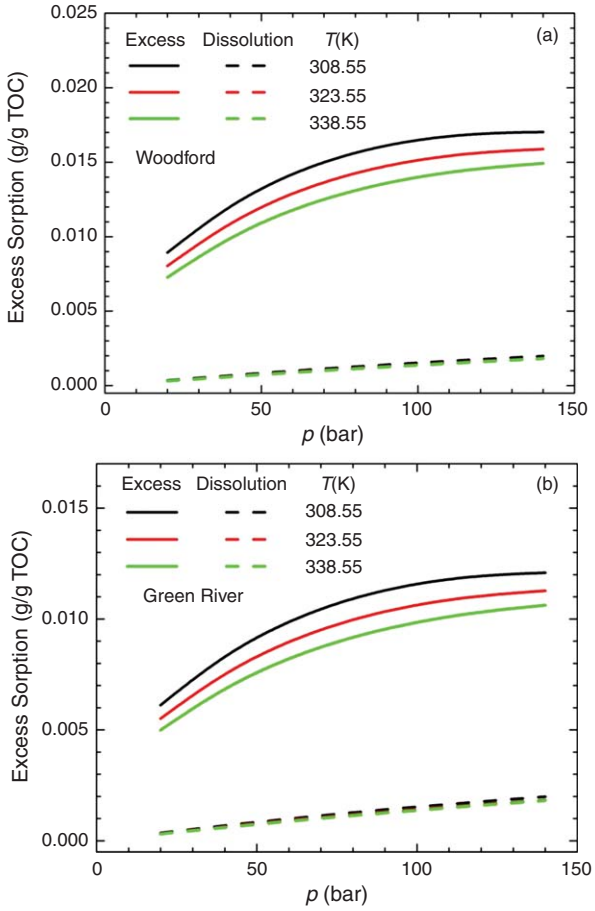

Fig. 20—Excess sorption and dissolution of C_1 in isolated kerogen from the (a) Woodford and, (b) Green River shale samples from the model at different temperatures.

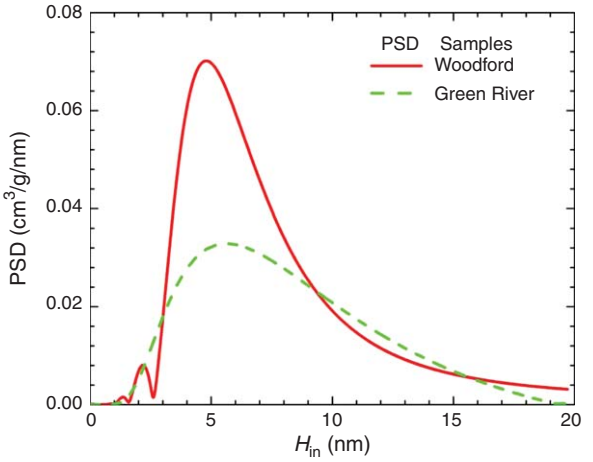

Fig. 21—PSDs of isolated kerogen from the Woodford and Green River shale samples.

$f_{g,0}^{G}$ = fugacity of pure gas component in gas phase
$f_{g,0}^{S}$ = fugacity of pure gas component in solid phase
f_S^g = fugacity of gas component in solid phase
$F[\rho(\mathbf{r})]$ = Helmholtz energy functional
H = slit-pore size
H_{in} = effective slit-pore size
M^G = molar weight of the gas phase
M^L = molar weight of the liquid phase
p = pressure
p_g^{boi} = pressure at the boiling-point T_g^{boi}
p^G = gas-phase pressure
p^L = liquid-phase pressure
p_g^{mel} = pressure at the melting-point T_g^{mel}
p_g^{sub} = pressure at the sublimation-point T_g^{sub}
P_c = capillary pressure
P_i = parachor of component i
r = radius of the pore
T = temperature
T_g^{boi} = boiling-point temperature of gas component
T_g^{mel} = melting-point temperature of gas component
T_g^{sub} = sublimation-point temperature of gas component
v_g = molar volume of gas component
x_g^S = mole fraction of gas component in solid phase
x_i = mole fraction of component i in the liquid phase
y_i = mole fraction of component i in the gas phase
γ_g^S = activity coefficient of gas component in kerogen
Γ_{ex}^a = measured excess sorption in nanopores
Γ_{ex}^s = gas dissolution in kerogen
Γ_{ex} = total excess sorption
Δ = interlayer spacing of graphite
Δh_g^{boi} = heat of vaporization of gas component
Δh_g^{mel} = heat of melting of gas component
Δh_g^{sub} = heat of sublimation of gas component
ε = attraction energy parameter
μ = chemical potential in outside reservoir
$\mu_{g,0}^G$ = chemical potential of pure gas component
$\mu_{g,0}^S$ = chemical potential of the pure superheated solid
μ_i^G = chemical potential of component i in the gas phase
μ_i^L = chemical potential of component i in the liquid phase
$\rho_{ave,ex}$ = excess sorption per unit inner pore volume
ρ_b = bulk density
$\rho(\mathbf{r})$ = density distribution at position $\mathbf{r}$
ρ_s = density of graphite
σ = surface tension
σ_g = diameter of species molecules
σ_s = diameter of surface molecules
$\varphi(\mathbf{r})$ = external potential at position $\mathbf{r}$
$\Omega[\rho(\mathbf{r})]$ = grand potential functional

Acknowledgments

This research was sponsored by the member companies of the Reservoir Engineering Research Institute. Their support is greatly appreciated.

References

Adesida, A. G., Akkutlu, I., Resasco, D. E. et al. 2011. Characterization of Barnett Shale Kerogen Pore Size Distribution Using DFT Analysis and Grand Canonical Monte Carlo Simulations. Presented at the SPE Annual Technical Conference and Exhibition, Denver, Colorado, USA, 30 October–2 November. SPE-147397-MS. http://dx.doi.org/10.2118/147397-MS.

Alharthy, N. S., Nguyen, T., Kazemi, H. et al. 2013. Multiphase Compositional Modeling in Small-Scale Pores of Unconventional Shale Reservoirs. Presented at the SPE Annual Technical Conference and Exhibition, New Orleans, Louisiana, USA, 30 September–2 October. SPE-166306-MS. http://dx.doi.org/10.2118/166306-MS.

Ambrose, R. J. 2011. *Micro-Structure of Gas Shales and Its Effects on Gas Storage and Production Performance*. PhD dissertation, Petroleum and Geological Engineering. Norman, Oklahoma (May 2011).

Ambrose, R. J., Hartman, R. C., Campos, M. D. et al. 2010. New Pore-scale Considerations for Shale Gas in Place Calculations. Presented at the SPE Unconventional Gas Conference, Pittsburgh, Pennsylvania, USA, 23–25 February. SPE-131772-MS. http://dx.doi.org/10.2118/131772-MS.

Amin, R. and Smith, T. N. 1998. Interfacial Tension and Spreading Coefficient Under Reservoir Conditions. *Fluid Phase Equilibria* **142** (1–2): 231–241. http://dx.doi.org/10.1016/S0378-3812(97)00213-6.

Balbuena, P. B. and Gubbins, K. E. 1993. Theoretical Interpretation of Adsorption Behavior of Simple Fluids in Slit Pores. *Langmuir* **9** (7): 1801–1814. http://dx.doi.org/10.1021/la00031a031.

Bruno, E., Marini Bettolo Marconi, U., and Evans, R. 1987. Phase Transitions in a Confined Lattice Gas: Prewetting and Capillary Condensation. *Physica A: Statistical Mechanics and Its Applications* **141** (1): 187–210. http://dx.doi.org/10.1016/0378-4371(87)90268-8.

Campos, M. D., Akkutlu, I. Y., and Sigal, R. F. 2009. A Molecular Dynamics Study on Natural Gas Solubility Enhancement in Water Confined to Small Pores. Presented at the SPE Annual Technical Conference and Exhibition, New Orleans, 47 October. SPE-124491-MS. http://dx.doi.org/10.2118/124491-MS.

Chen, X., Han, G., Han, A. et al. 2008. Nanoscale Fluid Transport: Size and Rate Effects. *Nano Letters* **8** (9): 2988–2992. http://dx.doi.org/10.1021/nl802046b.

Colwell, J. H., Gill, E. K., and Morrison, J. A. 1963. Thermodynamic Properties of CH4 and CD4. Interpretation of the Properties of the Solids. *J. Chemical Physics* **39** (3): 635–653. http://dx.doi.org/10.1063/1.1734303.

Das, M. and Jonk, R. 2012. Effect of Multicomponent Adsorption/Desorption Behavior on Gas-In-Place (GIP) and Estimated Ultimate Recovery (EUR) in Shale Gas Systems. Presented at the SPE Annual Technical Conference and Exhibition. San Antonio, Texas, USA, 8–10 October. SPE-159558-MS. http://dx.doi.org/10.2118/159558-MS.

Devegowda, D., Sapmanee, K., Civan, F. et al. 2012. Phase Behavior of Gas Condensates in Shales Due to Pore Proximity Effects: Implications for Transport Reserves and Well Productivity. Presented at the SPE Annual Technical Conference and Exhibition, San Antonio, Texas, USA, 8–10 October. SPE-160099-MS. http://dx.doi.org/10.2118/160099-MS.

Didar, B. R. and Akkutlu, I. Y. 2013. Pore-size Dependence of Fluid Phase Behavior and Properties in Organic-Rich Shale Reservoirs. Presented at the SPE International Symposium on Oilfield Chemistry. The Woodlands, Texas, USA, 8–10 April. SPE-164099-MS. http://dx.doi.org/10.2118/164099-MS.

Domalski, E. S. and Hearing, E. D. 1996. Heat Capacities and Entropies of Organic Compounds in the Condensed Phase. Volume III. *J. Physical and Chemical Reference Data* **25** (1): 1–525. http://dx.doi.org/10.1063/1.555985.

Dreisbach, F., Staudt, R., and Keller, J. U. 1999. High-Pressure Adsorption Data of Methane, Nitrogen, Carbon Dioxide and Their Binary and Ternary Mixtures on Activated Carbon. *Adsorption* **5** (3): 215–227. http://dx.doi.org/10.1023/A:1008914703884.

Du, L. and Chu, L. 2012. Understanding Anomalous Phase Behavior in Unconventional Oil Reservoirs. Presented at the SPE Canadian Unconventional Resources Conference. Calgary, Alberta, Canada, 30 October–1 November. SPE-161830-MS. http://dx.doi.org/10.2118/161830-MS.

Ebner, C. and Saam, W. F. 1977. New Phase-Transition Phenomena in Thin Argon Films. *Physical Review Letters* **38** (25): 1486–1489. http://dx.doi.org/10.1103/PhysRevLett.38.1486.

Ebner, C., Saam, W. F., and Stroud, D. 1976. Density-Functional Theory of Simple Classical Fluids. I. Surfaces. *Physical Review A* **14** (6): 2264–2273. http://dx.doi.org/10.1103/PhysRevA.14.2264.

Errington, J. R. and Panagiotopoulos, A. Z. 1999. A New Intermolecular Potential Model for the *n*-Alkane Homologous Series. *J. Physical Chemistry B* **103** (30): 6314–6322. http://dx.doi.org/10.1021/jp990988n.

Ertas, D., Kelemen, S. R., and Halsey, T. C. 2006. Petroleum Expulsion Part 1. Theory of Kerogen Swelling in Multicomponent Solvents. *Energy & Fuels* **20** (1): 295–300. http://dx.doi.org/10.1021/ef058024k.

Espinoza, D. N. and Santamarina, J. C. 2010. Water-CO2-Mineral Systems: Interfacial Tension, Contact Angle, and Diffusion—Implications to CO2 Geological Storage. *Water Resources Research* **46** (7): W07537. http://dx.doi.org/10.1029/2009WR008634.

Etminan, S. R., Javadpour, F., Maini, B. B. et al. 2014. Measurement of Gas Storage Processes in Shale and of the Molecular Diffusion Coefficient in Kerogen. *International J. Coal Geology* **123:** 10–19. http://dx.doi.org/10.1016/j.coal.2013.10.007.

Evans, R., Marini Bettolo Marconi, U., and Tarazona, P. 1986a. Capillary Condensation and Adsorption in Cylindrical and Slit-Like Pores. *J. Chemical Society, Faraday Trans. 2: Molecular and Chemical Physics* **82** (10): 1763–1787. http://dx.doi.org/10.1039/F29868201763.

Evans, R., Marini Bettolo Marconi, U., and Tarazona, P. 1986b. Fluids in Narrow Pores: Adsorption, Capillary Condensation, and Critical Points. *J. Chemical Physics* **84** (4): 2376–2399. http://dx.doi.org/10.1063/1.450352.

Evans, R. and Tarazona, P. 1984. Theory of Condensation in Narrow Capillaries. *Physical Review Letters* **52** (7): 557–560. http://dx.doi.org/10.1103/PhysRevLett.52.557.

Firoozabadi, A. 1999. *Thermodynamics of Hydrocarbon Reservoirs*. New York: McGraw-Hill.

Fisher, L. R. and Israelachvili, J. N. 1981. Experimental Studies on the Applicability of the Kelvin Equation to Highly Curved Concave Menisci. *J. Colloid and Interface Science* **80** (2): 528–541. http://dx.doi.org/10.1016/0021-9797(81)90212-5.

Flory, P. J. and Rehner, J. 1943. Statistical Mechanics of Cross-1 Polymer Networks II. Swelling. *J. Chemical Physics* **11** (11): 521–526. http://dx.doi.org/10.1063/1.1723792.

Gasparik, M., Bertier, P., Gensterblum, Y. et al. 2013. Geological Controls on the Methane Storage Capacity in Organic-Rich Shales. *International J. Coal Geology* **123:** 34–51. http://dx.doi.org/10.1016/j.coal.2013.06.010.

Gasparik, M., Ghanizadeh, A., Bertier, P. et al. 2012. High-Pressure Methane Sorption Isotherms of Black Shales From The Netherlands. *Energy & Fuels* **26** (8): 4995–5004. http://dx.doi.org/10.1021/ef300405g.

Giauque, W. F. and Egan, C. J. 1937. Carbon Dioxide. The Heat Capacity and Vapor Pressure of the Solid. The Heat of Sublimation. Thermodynamic and Spectroscopic Values of the Entropy. *J. Chemical Physics* **5** (1): 45–54. http://dx.doi.org/10.1063/1.1749929.

Heller, R. J. and Zoback, M. D. 2014. Adsorption of Methane and Carbon Dioxide on Gas Shale and Pure Mineral Samples. *J. Unconventional Oil and Gas Resources* **8**: 14–24. http://dx.doi.org/10.1016/j.juogr.2014.06.001.

Hensen, E. J. M., Tambach, T. J., Bliek, A. et al. 2001. Adsorption Isotherms of Water in Li–, Na–, and K–Montmorillonite by Molecular Simulation. *J. Chemical Physics* **115** (7): 3322–3329. http://dx.doi.org/10.1063/1.1386436.

Jäger, A. and Span, R. 2012. Equation of State for Solid Carbon Dioxide Based on the Gibbs Free Energy. *J. Chemical & Engineering Data* **57** (2): 590–597. http://dx.doi.org/10.1021/je2011677.

Jamaluddin, A. K. M., Kalogerakis, N. E., and Chakma, A. 1991. Predictions of Co2 Solubility and CO2 Saturated Liquid Density of Heavy Oils and Bitumens Using a Cubic Equation of State. *Fluid Phase Equilibria* **64**: 33–48. http://dx.doi.org/10.2118/10.1016/0378-3812(91)90004-Q.

Jhaveri, B. S. and Youngren, G. K. 1988. Three-Parameter Modification of the Peng-Robinson Equation of State To Improve Volumetric Predictions. *SPE Res Eval & Eng* **3** (3): 1033–1040. SPE-13118-PA. http://dx.doi.org/10.2118/13118-PA.

Ji, L., Zhang, T., Milliken, K. L. et al. 2012. Experimental Investigation of Main Controls to Methane Adsorption in Clay-Rich Rocks. *Applied Geochemistry* **27** (12): 2533–2545. http://dx.doi.org/10.1016/j.apgeochem.2012.08.027.

Jiménez-Ángeles, F. and Firoozabadi, A. 2014. Nucleation of Methane Hydrates at Moderate Subcooling by Molecular Dynamics Simulations. *J. Physical Chemistry C* **118** (21): 11310–11318. http://dx.doi.org/10.1021/jp5002012.

Jin, L., Yixin, M., and Jamili, A. 2013. Investigating the Effect of Pore Proximity on Phase Behavior and Fluid Properties in Shale Formations. Presented at the SPE Annual Technical Conference and Exhibition, New Orleans, Louisiana, USA, 30 September–2 October. SPE-166192-MS. http://dx.doi.org/10.2118/166192-MS.

Jin, Z. and Firoozabadi, A. 2013. Methane and Carbon Dioxide Adsorption in Clay-Like Slit Pores by Monte Carlo Simulations. *Fluid Phase Equilibria* **360:** 456–465. http://dx.doi.org/10.1016/j.fluid.2013.09.047.

Jin, Z. and Firoozabadi, A. 2014. Effect of Water on Methane and Carbon Dioxide Sorption in Clay Minerals by Monte Carlo Simulations. *Fluid*

Phase Equilibria **382:** 10–20. http://dx.doi.org/10.1016/j.fluid.2014.07.035.

Kanda, H., Miyahara, M., and Higashitani, K. 2004. Triple Point of Lennard-Jones Fluid in Slit Nanopore: Solidification of Critical Condensate. *J. Chemical Physics* **120** (13): 6173–6179. http://dx.doi.org/10.1063/1.1652431.

Kelemen, S. R., Walters, C. C., Ertas, D. et al. 2006. Petroleum Expulsion Part 2. Organic Matter Type and Maturity Effects on Kerogen Swelling by Solvents and Thermodynamic Parameters for Kerogen From Regular Solution Theory. *Energy & Fuels* **20** (1): 301–308. http://dx.doi.org/10.1021/ef0580220.

Kuila, U. and Prasad, M. 2011. Understanding Pore-Structure and Permeability in Shales. Presented at the SPE Annual Technical Conference and Exhibition. Denver, Colorado, USA, 30 October–2 November. SPE-146869-MS. http://dx.doi.org/10.2118/146869-MS.

Larsen, J. W. 2004. The Effects of Dissolved CO2 on Coal Structure and Properties. *International J. Coal Geology* **57** (1): 63–70. http://dx.doi.org/10.1016/j.coal.2003.08.001.

Larsen, J. W. and Li, S. 1994. Solvent Swelling Studies of Green River Kerogen. *Energy & Fuels* **8** (4): 932–936. http://dx.doi.org/10.1021/ef00046a017.

Larsen, J. W. and Li, S. 1997a. An Initial Comparison of the Interactions of Type I and III Kerogens With Organic Liquids. *Organic Geochemistry* **26** (5–6): 305–309. http://dx.doi.org/10.1016/S0146-6380(97)00016-8.

Larsen, J. W. and Li, S. 1997b. Changes in the Macromolecular Structure of a Type I Kerogen During Maturation. *Energy & Fuels* **11** (4): 897–901. http://dx.doi.org/10.1021/ef970007a.

Leahy-Dios, A., Das, M., Agarwal, A. et al. 2011. Modeling of Transport Phenomena and Multicomponent Sorption for Shale Gas and Coalbed Methane in an Unstructured Grid Simulator. Presented at the SPE Annual Technical Conference and Exhibition, Denver, Colorado, USA, 30 October–2 November. SPE-147352-MS. http://dx.doi.org/10.2118/147352-MS.

Leelavanichkul, P. 2003. *Crude Oil Characterization and Thermodynamic Modeling of Solids Precipitation in Crude Oils*. PhD thesis. Chemical Engineering. Salt Lake City, Utah, University of Utah (May 2003).

Lev, D. G., Gubbins, K. E., Radhakrishnan, R. et al. 1999. Phase Separation in Confined Systems. *Reports on Progress in Physics* **62** (12): 1573–1659. http://dx.doi.org/10.1088/0034-4885/62/12/201.

Li, Z. and Firoozabadi, A. 2009a. Interfacial Tension of Nonassociating Pure Substances and Binary Mixtures by Density Functional Theory Combined With Peng–Robinson Equation of State. *J. of Chemical Physics* **130** (15): 154108. http://dx.doi.org/10.1063/1.3100237.

Li, Z. and Firoozabadi, A. 2009b. Cubic-Plus-Association Equation of State for Water-Containing Mixtures: Is "Cross Association" Necessary?" *AIChE J.* **55** (7): 1803–1813. http://dx.doi.org/10.1002/aic.11784.

Li, Z., Jin, Z., and Firoozabadi, A. 2014. Phase Behavior and Adsorption of Pure Substances and Mixtures and Characterization in Nanopore Structures by Density Functional Theory. *SPE J.* **19** (6): 1096–1109. SPE-169819-PA. http://dx.doi.org/10.2118/169819-PA.

Liu, Y. and Wilcox, J. 2012. Molecular Simulation of CO2 Adsorption on Micro- and Mesoporous Carbons With Surface Heterogeneity. *International J. Coal Geology* **104:** 83–95. http://dx.doi.org/10.1016/j.coal.2012.04.007.

Lu, X.-C., Li, F.-C., and Watson, A. T. 1995. Adsorption Measurements in Devonian Shales. *Fuel* **74** (4): 599–603. http://dx.doi.org/10.1016/0016-2361(95)98364-K.

Majer, V. and Kehiaian, H. V. 1985. *Enthalpies of Vaporization of Organic Compounds: A Critical Review and Data Compilation*. Oxford: Blackwell Scientific Ltd.

Manger, K. C., Oliver, S. J. P., Curtis, J. B. et al. 1991. Geologic Influences on the Location and Production of Antrim Shale Gas, Michigan Basin. Presented at the Low-Permeability Reservoirs Symposium. Denver, Colorado, USA, 15–17 April. SPE-21854-MS. http://dx.doi.org/10.2118/21854-MS.

Martin, M. G. and Siepmann, J. I. 1998. Transferable Potentials for Phase Equilibria. 1. United-Atom Description of *n*-Alkanes. *J. Physical Chemistry B* **102** (14): 2569–2577. http:/dx.doi.org/10.1021/jp972543+.

Mehrotra, A. K., Patience, G. S., and Svrcek, W. Y. 1989. Calculation of Gas Solubility in Wabasca Bitumen. *J Can Pet Technol* **28** (3): 81–83. SPE-89-03-08-PA. http://dx.doi.org/10.2118/89-03-08-PA.

Mehrotra, A. K., Sarkar, M., and Svrcek, W. Y. 1985. Bitumen Density and Gas Solubility Predictions Using the Peng-Robinson Equation of State. *AOSTRA J. Research* **1** (4): 215–229.

Mehrotra, A. K. and Svrcek, W. Y. 1982. Correlations for Properties of Bitumen Saturated With CO2, CH4 And N2, and Experiments With Combustion Gas Mixtures. *J Can Pet Technol* **21** (6): 95–104. SPE-82-06-05-PA. http://dx.doi.org/10.2118/82-06-05-PA.

Mehrotra, A. K. and Svrcek, W. Y. 1988. Characterization of Athabasca Bitumen for Gas Solubility Calculations. *J Can Pet Technol* **27** (6): 107–110. SPE-88-06-09-PA. http://dx.doi.org/10.2118/88-06-09-PA.

Morishige, K., Fujii, H., Uga, M. et al. 1997. Capillary Critical Point of Argon, Nitrogen, Oxygen, Ethylene, and Carbon Dioxide in MCM-41. *Langmuir* **13** (13): 3494–3498. http://dx.doi.org/10.1021/la970079u.

Nagarajan, N. and Robinson, R. L. 1986. Equilibrium Phase Compositions, Phase Densities, and Interfacial Tensions for Carbon Dioxide + Hydrocarbon Systems. 2. Carbon Dioxide + *N*-Decane. *J. Chemical & Engineering Data* **31** (2): 168–171. http://dx.doi.org/10.1021/je00044a012.

Nojabaei, B., Johns, R. T., and Chu, L. 2013. Effect of Capillary Pressure on Phase Behavior in Tight Rocks and Shales. *SPE Res Eval & Eng* **16** (3): 281–289. SPE-159258-PA. http://dx.doi.org/10.2118/159258-PA.

Olivier, J. 1995. Modeling Physical Adsorption on Porous and Nonporous Solids Using Density Functional Theory. *J. Porous Materials* **2** (1): 9–17. http://dx.doi.org/10.1007/BF00486565.

Ottiger, S., Pini, R., Storti, G. et al. 2008. Competitive Adsorption Equilibria of CO2 and CH4 on a Dry Coal. *Adsorption* **14** (4–5): 539–556. http://dx.doi.org/10.1007/s10450-008-9114-0.

Pan, H. and Firoozabadi, A. 1998. Thermodynamic Micellization Model for Asphaltene Aggregation and Precipitation in Petroleum Fluids. *SPE Prod & Fac* **13** (2): 118–127. SPE-36741-PA. http://dx.doi.org/10.2118/36741-PA.

Peng, D.-Y. and Robinson, D. B. 1976. A New Two-Constant Equation of State. *Industrial & Engineering Chemistry Fundamentals* **15** (1): 59–64. http://dx.doi.org/10.1021/i160057a011.

Ravikovitch, P. I., Vishnyakov, A., Russo, R. et al. 2000. Unified Approach to Pore Size Characterization of Microporous Carbonaceous Materials from N2, Ar, and CO2 Adsorption Isotherms†. *Langmuir* **16** (5): 2311–2320. http://dx.doi.org/10.1021/la991011c.

Reyes, Y. 2012. Vapor–Liquid Phase Diagrams and Structure of a Square-Well Fluid Confined in Weakly Attractive Cylindrical Pores. *Fluid Phase Equilibria* **336:** 28–33. http://dx.doi.org/10.1016/j.fluid.2012.06.033.

Riazi, M. R. and Al-Sahhaf, T. A. 1996. Physical Properties of Heavy Petroleum Fractions and Crude Oils. *Fluid Phase Equilibria* **117** (1–2): 217–224. http://dx.doi.org/10.1016/0378-3812(95)02956-7.

Robinson, D. B., Peng, D.-Y., and Chung, S. Y-K, 1985. The Development of the Peng-Robinson Equation and Its Application to Phase Equilibrium in a System Containing Methanol. *Fluid Phase Equilibria* **24** (1–2): 25–41. http://dx.doi.org/10.1016/0378-3812(85)87035-7.

Rosenfeld, Y. 1989. Free-Energy Model for the Inhomogeneous Hard-Sphere Fluid Mixture and Density-Functional Theory of Freezing. *Physical Review Letters* **63** (9): 980–983. http://dx.doi.org/10.1103/PhysRevLett.63.980.

Ross, D. J. K. and Bustin, R. M. 2007. Shale Gas Potential of the Lower Jurassic Gordondale Member, Northeastern British Columbia, Canada. *Bull. Canadian Petroleum Geology* **55** (1): 51–75. http://dx.doi.org/10.2113/gscpgbull.55.1.51.

Ross, D. J. K. and Bustin, R. 2009. The Importance of Shale Composition and Pore Structure Upon Gas Storage Potential of Shale Gas Reservoirs. *Marine and Petroleum Geology* **26** (6): 916–927. http://dx.doi.org/10.1016/j.marpetgeo.2008.06.004.

Rowlinson, J. S. and Swinton, F. L. 1982. *Liquids and Liquid Mixtures*. London: Butterworth.

Rowlinson, J. S. and Widom, B. 1982. *Molecular Theory of Capillarity*. Oxford: Clarendon.

Sapmanee, K. 2011. *Effects of Pore Proximity on Behavior and Production Prediction of Gas/Condensate*. Master's thesis, University of Oklahoma (May 2011).

Singh, S. K., Sinha, A., Deo, G. et al. 2009. Vapor-Liquid Phase Coexistence, Critical Properties, and Surface Tension of Confined Alkanes. *J. Physical Chemistry C* **113** (17): 7170–7180. http://dx.doi.org/10.1021/jp8073915.

Smit, B., Karaborni, S., and Siepmann, J. I. 1995. Computer Simulations of Vapor–Liquid Phase Equilibria of *N*-Alkanes. *J. Chemical Physics* **102** (5): 2126–2140. http://dx.doi.org/10.1063/1.469563.

Steele, W. A. 1973. The Physical Interaction of Gases With Crystalline Solids: I. Gas-Solid Energies and Properties of Isolated Adsorbed Atoms. *Surface Science* **36** (1): 317–352. http://dx.doi.org/10.1016/0039-6028(73)90264-1.

Strapoc, D., Mastalerz, M., Schimmelmann, A. et al. 2010. Geochemical Constraints on the Origin and Volume of Gas in the New Albany Shale (Devonian-Mississippian), Eastern Illinois Basin. *AAPG Bull.* **94** (11): 1713–1740. http://dx.doi.org/10.1306/06301009197.

Svrcek, W. Y. and Mehrotra, A. K. 1982. Gas Solubility, Viscosity and Density Measurements for Athabasca Bitumen. *J Can Pet Technol* **21** (4): 31–38. SPE-82-04-02-PA. http://dx.doi.org/10.2118/82-04-02-PA.

Tomsik, T. M., Johnson, W. L., Smudde, T. D. et al. 2010. *A Densified Liquid Methane Delivery System for the Altair Ascent Stage*. Huntsville, Alabama: NASA.

Travalloni, L., Castier, M., Tavares, F. W. et al. 2010. Critical Behavior of Pure Confined Fluids From an Extension of the Van Der Waals Equation of State. *J. Supercritical Fluids* **55** (2): 455–461. http://dx.doi.org/10.1016/j.supflu.2010.09.008.

Trebin, F. A. and Zadora, G. I. 1968. Experimental Study of the Effect of Porous Media on Phase Changes in Gas Condensate Systems. *Neft' i Gaz* **81:** 37–52.

van der Ploeg, P. and Berendsen, H. J. C. 1982. Molecular Dynamics Simulation of a Bilayer Membrane. *J. Chemical Physics* **76** (6): 3271–3276. http://dx.doi.org/10.1063/1.443321.

Varet, G., Montel, F., Nasri, D. et al. 2013. Gas Solubility Measurement in Heavy Oil and Extra Heavy Oil at Vapor Extraction (VAPEX) Conditions. *Energy & Fuels* **27** (5): 2528–2535. http://dx.doi.org/10.1021/ef400266t.

Vermylen, J. P. 2011. *Geomechanical Studies of the Barnett Shale, Texas, USA*. PhD thesis, Department of Geophysics. Stanford, California, Stanford University (May 2011).

Wang, W., Wu, K., Duan, J. et al. 2013a. Thermodynamics Prediction of Wax Precipitation in Black Oil Using Regular Solution Model and Plus Fraction Characterization. *Advances in Mechanical Engineering* **2013:** 1–8. http://dx.doi.org/10.1155/2013/829591.

Wang, Y., Yan, B., and Killough, J. 2013b. Compositional Modeling of Tight Oil Using Dynamic Nanopore Properties. Presented at the SPE Annual Technical Conference and Exhibition. New Orleans, Louisiana, USA, 30 September–2 October. SPE-166267-MS. http://dx.doi.org/10.2118/166267-MS.

Weinaug, C. F. and Katz, D. L. 1943. Surface Tensions of Methane-Propane Mixtures. *Industrial & Engineering Chemistry* **35** (2): 239–246. http://dx.doi.org/10.1021/ie50398a028.

Weniger, P., Kalkreuth, W., Busch, A. et al. 2010. High-Pressure Methane and Carbon Dioxide Sorption on Coal and Shale Samples From the Paraná Basin, Brazil. *International J. Coal Geology* **84** (3–4): 190–205. http://dx.doi.org/10.1016/j.coal.2010.08.003.

Widom, B. 1963. Some Topics in the Theory of Fluids. *J. Chemical Physics* **39** (11): 2808–2812. http://dx.doi.org/10.1063/1.1734110.

Won, K. W. 1986. Thermodynamics for Solid Solution-Liquid-Vapor Equilibria: Wax Phase Formation From Heavy Hydrocarbon Mixtures. *Fluid Phase Equilibria* **30:** 265–279. http://dx.doi.org/10.1016/0378-3812(86)80061-9.

Zarragoicoechea, G. J. and Kuz, V. A. 2004. Critical Shift of a Confined Fluid in a Nanopore. *Fluid Phase Equilibria* **220** (1): 7–9. http://dx.doi.org/10.1016/j.fluid.2004.02.014.

Zhang, T., Ellis, G. S., Ruppel, S. C. et al. 2012. Effect of Organic-Matter Type and Thermal Maturity on Methane Adsorption in Shale-Gas Systems. *Organic Geochemistry* **47:** 120–131. http://dx.doi.org/10.1016/j.orggeochem.2012.03.012.

Zhang, Y., Civan, F., Devegowda, D. et al. 2013. Improved Prediction of Multi-Component Hydrocarbon Fluid Properties in Organic Rich Shale Reservoirs. Presented at the SPE Annual Technical Conference and Exhibition, New Orleans, Louisiana, USA, 30 September–2 October. SPE-166290-MS. http://dx.doi.org/10.2118/166290-MS.

Appendix A: Comparison Between the Peng-Robinson Equation-of-State (PR-EOS) Calculations and Experimental Data on Dissolution of a Single-Component Gas in Bitumen Liquid

The comparison between the PR-EOS calculations and experimental data is shown in **Fig. A-1.** The agreement between the results from the PR-EOS and experimental data is very good.

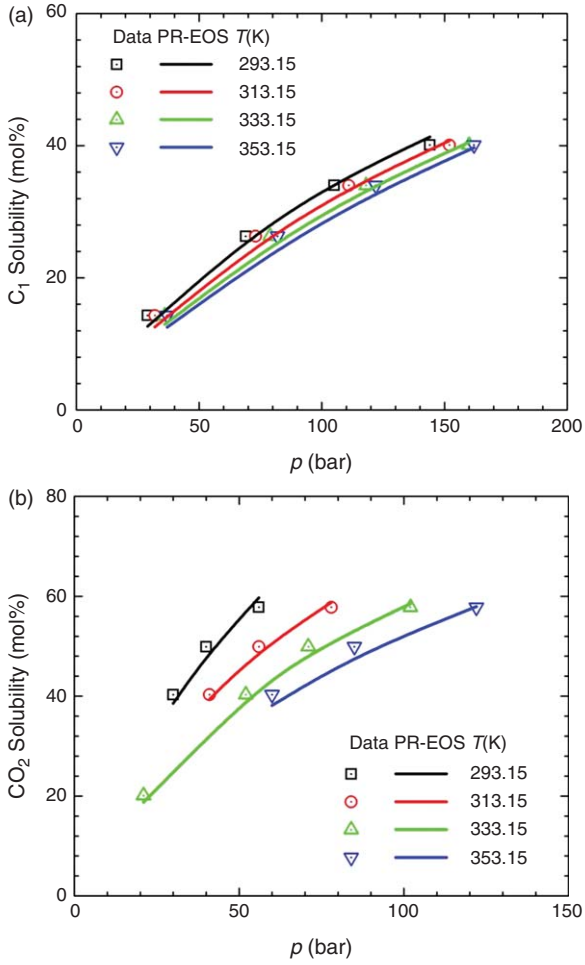

Fig. A-1—(a) C_1 and (b) CO_2 solubility in Athabasca bitumen at various temperatures from the PR-EOS calculation and experimental data (Varet et al. 2013).

Appendix B: Fugacity of Pure Superheated Solid Phase

To obtain the chemical potential difference between pure fluids at (T, p) in different phase states, we construct a thermodynamic cycle, as shown in **Fig. B-1** for C_1 and in **Fig. B-2** for CO_2. Superheated C_1 in solid phase passes through the melting and boiling points to the gas phase; superheated CO_2 in solid phase passes through the sublimation point directly to the gas phase.

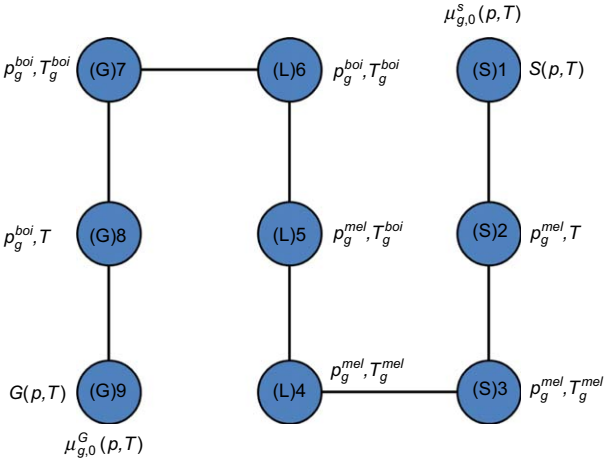

Fig. B-1—Thermodynamic cycle for C_1 from superheated solid phase to vapor phase. p_g^{mel} is the pressure at the melting-point temperature T_g^{mel}, and p_g^{boi} is the pressure at the boiling-point temperature T_g^{boi}.

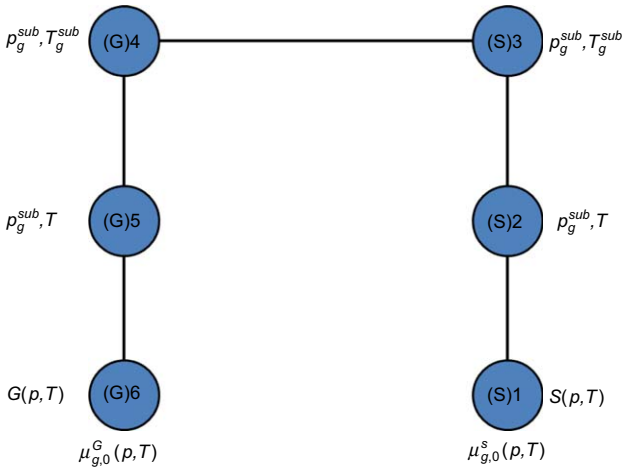

Fig. B-2—Thermodynamic cycle for CO_2 from superheated solid phase to vapor phase. p_g^{sub} is the pressure at the sublimation-point temperature T_g^{sub}.

The fugacity of pure C_1 in superheated solid state is given by

$$f^S_{g,0}(p,T) = f^G_{g,0}(p,T) \times \exp\left\{ -\frac{1}{RT}\left[\int_p^{p_g^{mel}} v_g^S(P)\mathrm{d}P + \int_{p_g^{mel}}^{p_g^{boi}} v_g^L(P)\mathrm{d}P + \int_{p_g^{boi}}^{p} v_g^G(P)\mathrm{d}P + \int_T^{T_g^{mel}} C^S_{g,p}(T)\mathrm{d}T - T\int_T^{T_g^{mel}} \frac{C^S_{g,p}(T)}{T}\mathrm{d}T + \int_{T_g^{mel}}^{T_g^{boi}} C^L_{g,p}(T)\mathrm{d}T - T\int_{T_g^{mel}}^{T_g^{boi}} \frac{C^L_{g,p}(T)}{T}\mathrm{d}T + \int_{T_g^{boi}}^{T} C^G_{g,p}(T)\mathrm{d}T - T\int_{T_g^{boi}}^{T} \frac{C^G_{g,p}(T)}{T}\mathrm{d}T + \Delta h_g^{mel}\left(1-\frac{T}{T_g^{mel}}\right) + \Delta h_g^{boi}\left(1-\frac{T}{T_g^{boi}}\right)\right]\right\}, \quad \cdots\cdots\cdots\cdots (B\text{-}1)$$

where p_g^{mel} is the pressure at the melting-point temperature T_g^{mel}; p_g^{boi} is the pressure at the boiling-point temperature T_g^{boi}, v_g, $C_{g,P}$, Δh_g^{mel}, and Δh_g^{boi} are the molar volume, heat capacity, heat of melting, and heat of vaporization of gas component, respectively. Fugacity of pure CO_2 in superheated solid state is given by

$$f^S_{g,0}(p,T) = f^G_{g,0}(p,T) \times \exp\left\{ -\frac{1}{RT}\left[\int_p^{p_g^{sub}} v_g^S(P)\mathrm{d}P + \int_{p_g^{sub}}^{p} v_g^G(P)\mathrm{d}P + \Delta h_g^{sub}\left(1-\frac{T}{T_g^{sub}}\right) + \int_T^{T_g^{sub}} C^S_{g,p}(T)\mathrm{d}T - T\int_T^{T_g^{sub}} \frac{C^S_{g,p}(T)}{T}\mathrm{d}T + \int_{T_g^{sub}}^{T} C^G_{g,p}(T)\mathrm{d}T - T\int_{T_g^{sub}}^{T} \frac{C^G_{g,p}(T)}{T}\mathrm{d}T\right]\right\}, \quad \cdots\cdots\cdots (B\text{-}2)$$

in which p_g^{sub} is the pressure at the sublimation-point temperature T_g^{sub} and Δh_g^{sub} is the heat of sublimation, respectively (Leelavanichkul 2003).

$C_{g,p}$ and v_g of the liquid and vapor phases are obtained from the National Institute of Standards and Technology webbook. We assume v_g in solid state to be independent of pressure. Because data for $C_{g,p}$ for solid phase are only available at low temperature, we use $C^S_{g,p}$ at melting point for C_1 (Colwell et al. 1963) and at sublimation point for CO_2 (Giauque and Egan 1937; Jäger and Span 2012) in Eqs. B-1 and B-2, respectively. The relevant parameters for C_1 and CO_2 are listed in **Table B-1.** The density of dry ice varies between approximately 1.4 and 1.6 g/cm^3. In this work, we assume that the density of solid CO_2 is 1.562 g/cm^3 (Riazi and Al-Sahhaf 1996).

C_1			
p_g^{fus} (bar)	p_g^{boi} (bar)	T_g^{fus} (K)	T_g^{boi} (K)
1.01325	1.01325	90.7 (Domalski and Hearing 1996)	111.7 (Majer and Kehiaian 1985)
Δh_g^{fus} (kJ/mol)	Δh_g^{boi} (kJ/mol)	$C^S_{g,p}$ (J/mol·K)	v_g^S (m^3/mol)
0.94 (Domalski and Hearing 1996)	8.17 (Majer and Kehiaian 1985)	44.10 (Colwell et al. 1963)	3.13953×10^{-5} (Tomsik et al. 2010)
CO_2			
p_g^{sub} (bar)	T_g^{sub} (K)	Δh_g^{sub} (kJ/mol)	$C^S_{g,P}$ (J/mol·K)
1.01325	194.67 (Giauque and Egan 1937)	25.23 (Giauque and Egan 1937)	55.0 (Giauque and Egan 1937)
v_g^S (m^3/mol)			
2.8174×10^{-5}			

Table B-1—Parameters for C_1 and CO_2 in dissolution calculations.

Appendix C: Activity Coefficient of Gas in Solid Solution

The activity coefficient γ_g^S of species g in solid solution is computed from (Won 1986)

$$\gamma_g^S = \frac{v_g(\overline{\delta^S} - \delta_g^S)^2}{RT}, \quad \ldots\ldots\ldots\ldots\ldots\ldots\ldots\ldots\ldots\ldots (C\text{-}1)$$

where

$$\overline{\delta^S} = \sum_i \phi_i^S \delta_i^S, \quad \ldots\ldots\ldots\ldots\ldots\ldots\ldots\ldots\ldots\ldots (C\text{-}2)$$

$$\phi_i^S = \frac{x_i^S v_i}{\sum_i x_i^S v_i}, \quad \ldots\ldots\ldots\ldots\ldots\ldots\ldots\ldots\ldots\ldots (C\text{-}3)$$

in which v_i is the molar volume of component i in cm^3/mol, δ_i^S is the solubility parameter of component i in solid solution in (calories/cm^3)$^{0.5}$, ϕ_i^S is the volume fraction of component i, and $\overline{\delta^S}$ is the average solubility parameter of solid solution. The solubility parameter in solid solution is related to the solubility parameter in liquid solution (Wang et al. 2013a)

$$\delta_i^S = \left[\frac{\Delta H_i^f}{v_i} + (\delta_i^L)^2\right]^{0.5}, \quad \ldots\ldots\ldots\ldots\ldots\ldots\ldots\ldots\ldots\ldots (C\text{-}4)$$

where ΔH_i^f is the heat of fusion of component i in calories/mol and δ_i^L is the solubility parameter in liquid solution of component i in (calories/cm^3)$^{0.5}$. The following correlation is used to calculate ΔH_i^f (Won 1986):

$$\Delta H_i^f = 0.1426 M_i T_i^f, \quad \ldots\ldots\ldots\ldots\ldots\ldots\ldots\ldots\ldots\ldots (C\text{-}5)$$

$$T_i^f = 374.5 + 0.02617 M_i - 20172/M_i, \quad \ldots\ldots\ldots\ldots\ldots\ldots\ldots\ldots\ldots\ldots (C\text{-}6)$$

where T_i^f and M_i are melting temperature in K and molecular weight in g/mol of component i, respectively. As in Won (1986), the ΔH_i^f of methane and CO_2 in Eq. C-4 is neglected. Solubility parameters of gas and C_7–C_{29} in kerogen in liquid solution are calculated from the correlation proposed by Riazi and Al-Sahhaf (1996),

$$\delta_i^L = 8.6 - \exp(2.219195 - 0.54907 M_i^{0.3}). \quad \ldots\ldots\ldots\ldots\ldots\ldots\ldots\ldots\ldots\ldots (C\text{-}7)$$

The solubility parameters of heavy component and asphalthene in kerogen in liquid solution are obtained from the correlation proposed by Leelavanichkul (2003),

$$\delta_{\text{heavy}}^L = 8.8 - \exp(2.219195 - 0.54907 M_{\text{heavy}}^{0.3}), \quad \ldots\ldots\ldots\ldots\ldots\ldots\ldots\ldots\ldots\ldots (C\text{-}8)$$

$$\delta_{\text{asph}}^L = 9.3 - \exp(2.219195 - 0.54907 M_{\text{asph}}^{0.3}). \quad \ldots\ldots\ldots\ldots\ldots\ldots\ldots\ldots\ldots\ldots (C\text{-}9)$$

The molar volume of component i, v_i, in Eq. C-4 is calculated by the following correlation:

$$d_i^L = 0.8155 + 0.6272 \times 10^{-4} M_i - 13.06/M_i, \quad \ldots\ldots\ldots\ldots\ldots\ldots\ldots\ldots\ldots\ldots (C\text{-}10)$$

$$v_i = M_i/d_i^L. \quad \ldots\ldots\ldots\ldots\ldots\ldots\ldots\ldots\ldots\ldots (C\text{-}11)$$

For gas component, we use molar volume in solid phase, as shown in Table B-1.

Fig. C-1 presents activity coefficients of C_1 and CO_2 in kerogen at different temperatures. The effect of pressure on activity coefficients of C_1 and CO_2 in kerogen is neglected.

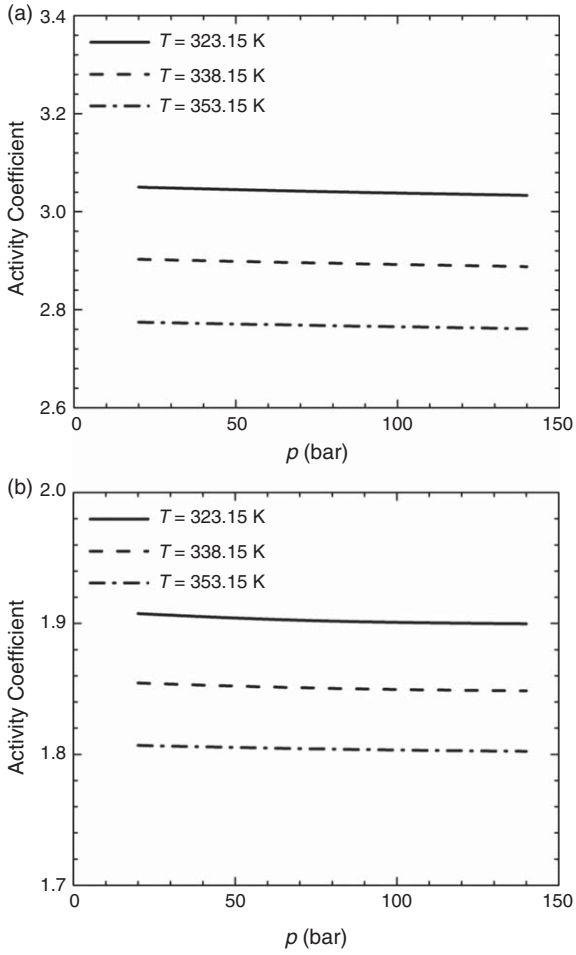

Fig. C-1—Activity coefficients of (a) C_1 and (b) CO_2 in kerogen at different temperatures.

Zhehui Jin is a researcher at Reservoir Engineering Research Institute (RERI). His current research interests include enhanced oil recovery (EOR) in gas injection, multiphase equilibrium computations, pressure/volume/temperature modeling, thermodynamics of fluids in nanoporous media, statistical thermodynamics modeling of phase behavior, and transport phenomena in shale gas reservoirs. Jin holds a BS degree in materials science and engineering from Tsinghua University and a PhD degree in chemical engineering from University of California, Riverside.

Abbas Firoozabadi is the senior scientist at RERI and a faculty member at Yale University. His research focus includes (1) molecular structure in petroleum fluid/rock systems with applications in low-salinity-water injection, shale-gas and light-oil reservoirs, improved oil recovery, and flow assurance and (2) higher-order reservoir simulation. Firoozabadi is the author of a forthcoming book *Thermodynamics and Applications in Hydrocarbon Energy Production* by McGraw-Hill. He is the recipient of the SPE Anthony Lucas Gold Medal and a member of the US National Academy of Engineering. Firoozabadi holds a BS degree from the Abadan Institute of Technology, Abadan, Iran, and MS and PhD degrees from the Illinois Institute of Technology, Chicago, Illinois, followed by a post-doctoral position at the University of Michigan. All degrees are in natural-gas engineering.